

# Revisiting daily MODIS evapotranspiration algorithm using flux tower measurements in China

Lei Huang<sup>1</sup>, Tammo S Steenhuis<sup>2</sup>, Yong Luo<sup>1</sup>, Qihong Tang<sup>3</sup>, Ronglin Tang<sup>4</sup>, Junqing Zheng<sup>1</sup>, Wen Shi<sup>1</sup>, and Chen Qiao<sup>1</sup>

<sup>1</sup>Tsinghua University

<sup>2</sup>Cornell University

<sup>3</sup>Institute of Geographic Sciences and Natural Resources Research, Chinese Academy of Sciences

<sup>4</sup>Institute of Geographical Science and Natural Resources Research

November 24, 2022

## Abstract

Evapotranspiration ( $ET$ ) is the major component of the hydrology cycle. Satellites provide a convenient way for gathering information to estimate regional  $ET$ . The most widely applied method for converting the instantaneous satellite measurement to daily scale assumes that evaporative fraction ( $EF$ ), defined as the ratio of  $ET$  to the available energy, is constant during the daytime. However, this method was proved to underestimate the daily  $ET$ . This study implemented a theoretically improved  $EF$  algorithm to calculate daily  $ET$  with the decoupling factor method based on the Penman-Monteith and McNaughton-Jarvis equations. Seven improved algorithms were developed by assuming that various parameters remain constant during the day. The satellite-based  $ET$  estimates were compared with seven local flux tower measurements in China. The results showed that: (1) The original  $ET$  method calculated the daily evaporation more accurately than the other algorithms. However, the good fit was based on two compensating inaccuracies. Compared to the flux tower measurement, the original  $ET$  method underestimated the daily  $EF$  by 26% and overestimated the daily net radiation by 30%. (2) Six of the seven proposed algorithms underpredicted the daily  $ET$  by 30-60%, mainly due to the inaccurate daily net radiation. (3) The algorithm that assumed that the instantaneous decoupling parameter  $\Omega^*$  was equal to its daily value method calculated  $EF$  and  $ET$  with the relative errors of 8% and 10% when the inaccurate estimated daily net radiation was replaced by the observed flux tower data.

1

# 1 **Revisiting daily MODIS evapotranspiration algorithm using flux tower**

2

## **measurements in China**

3 **Lei Huang<sup>1,2</sup>, Tammo S. Steenhuis<sup>2\*</sup>, Yong Luo<sup>1\*</sup>, Qihong Tang<sup>3,5</sup>, Ronglin**

4 **Tang<sup>4,5</sup>, Junqing Zheng<sup>1</sup>, Wen Shi<sup>1</sup> and Chen Qiao<sup>1</sup>**

5 <sup>1</sup>Ministry of Education Key Laboratory for Earth System Modeling, Department of  
6 Earth System Science, Tsinghua University, Beijing, China.

7 <sup>2</sup>Department of Biological and Environmental Engineering, Cornell University,  
8 Ithaca, NY, USA

9 <sup>3</sup>Key Laboratory of Water Cycle and Related Land Surface Processes, Institute of  
10 Geographic Sciences and Natural Resources Research, Chinese Academy of Sciences,  
11 Beijing, China.

12 <sup>4</sup>State Key Laboratory of Resources and Environment Information System, Institute of  
13 Geographic Sciences and Natural Resources Research, Chinese Academy of Sciences,  
14 Beijing 100101, China.

15 <sup>5</sup>University of Chinese Academy of Sciences, Beijing 100049, China.

16

17

18 Corresponding author: Tammo S. Steenhuis (tammo@cornell.edu)

19 Yong Luo (Yongluo@mail.tsinghua.edu.cn)

20

21

22 **Key Points:**

23 **Improved satellite-based daily evapotranspiration calculations for China**

24 **Decoupling parameter based daily evapotranspiration fraction algorithm**

25

26

2

3

**27 Abstract**

28 Evapotranspiration (*ET*) is the major component of the hydrology cycle. Satellites  
29 provide a convenient way for gathering information to estimate regional *ET*. The  
30 most widely applied method for converting the instantaneous satellite measurement to  
31 daily scale assumes that evaporative fraction (*EF*), defined as the ratio of *ET* to the  
32 available energy, is constant during the daytime. However, this method was proved to  
33 underestimate the daily *ET*. This study implemented a theoretically improved *EF*  
34 algorithm to calculate daily *ET* with the decoupling factor method based on the  
35 Penman-Monteith and McNaughton-Jarvis equations. Seven improved algorithms  
36 were developed by assuming that various parameters remain constant during the day.  
37 The satellite-based *ET* estimates were compared with seven local flux tower  
38 measurements in China. The results showed that: (1) The original *ET* method  
39 calculated the daily evaporation more accurately than the other algorithms. However,  
40 the good fit was based on two compensating inaccuracies. Compared to the flux tower  
41 measurement, the original *ET* method underestimated the daily *EF* by 26% and  
42 overestimated the daily net radiation by 30%. (2) Six of the seven proposed  
43 algorithms underpredicted the daily *ET* by 30-60%, mainly due to the inaccurate  
44 daily net radiation. (3) The algorithm that assumed that the instantaneous decoupling  
45 parameter  $\Omega^i$  was equal to its daily value method calculated *EF* and *ET* with the  
46 relative errors of 8% and 10% when the inaccurate estimated daily net radiation was  
47 replaced by the observed flux tower data.

**48 Plain Language Summary**

49 The water that evaporates from the land surface sustains the hydrological cycle that  
50 replenishes the world's freshwater resources. Scientists and water managers are  
51 therefore interested in quantifying the water that evaporates each day. It is especially  
52 true for China that has one of the lowest water reserves in the world. Satellites that  
53 provide coverage of all the land surface would be ideal for recording evaporation if  
54 we could scale up the instantaneous satellite measurements to a daily scale. The

55 current scale-up methods available have not been widely tested. In this manuscript,  
56 we test the available methods and show how they can be improved for China.

## 57 **1 Introduction**

58 In the seventeenth century, the first water balance was made for the Seine by  
59 Perrault (1674). Since that time, it became apparent that evapotranspiration (*ET*)  
60 sustains the hydrologic cycle and replenishes the world's freshwater resources (Katul  
61 and Novick, 2009). Today, evaporation is a critical component of the short-term  
62 numerical weather prediction, long-term climate simulations, and diagnoses of  
63 climate change (Brutsaert et al., 2019; Jung et al., 2019; Wang & Dickinson, 2012).

64 Products of actual evaporation are usually from ground measurements, climate  
65 (or hydrology) model output, or satellite-based estimates. Ground measurements like  
66 flux towers and lysimeters can make ground or point scale evaporation measurements.  
67 Pan evaporation can be used for point scale but needs to be adjusted for the soil  
68 moisture content using a model such as the Thornthwaite Water Procedure (Portela et  
69 al., 2019; Steenhuis & van der Molen, 1982). The climate and hydrology models  
70 could provide large-scale and long-time *ET* estimates, but they often have coarse  
71 resolutions and assuming the land cover was fixed, leading to large uncertainties.  
72 Satellite measurements can calculate regional-scale evaporation at low-cost (Miranda  
73 et al., 2017), and unlike the climate models, they have higher resolution and more  
74 realistic land parameters. Moderate Resolution Imaging Spectroradiometer (MODIS)  
75 (Ait Hssaine et al., 2020; Faisal et al., 2020; Mu et al., 2007, 2011; Zhang et al.,  
76 2019), Advanced Very High-Resolution Radiometer (AVHRR) (Dile et al., 2020;  
77 Zhang et al., 2009, 2010) and Landsat (Allen Richard G. et al., 2007; Bastiaanssen,  
78 Menenti, et al., 1998; Bastiaanssen, Paul, et al., 2020) have tabulated over the past 20  
79 years, and they provided pioneering satellite-based regional *ET* estimates models.

80 Evapotranspiration for large basins or countries by remote sensing methods is  
81 calculated by extrapolating instantaneous remotely sensed satellite measurements  
82 (usually taken around midday) over daily or more extended periods (Hou et al., 2019;  
83 Zou et al., 2018). Several published methods convert the instantaneous *ET*

84 measurements to the daily evaporation: constant evaporative fraction method  
85 (Brutsaert & Sugita, 1992), reference evaporative fraction method (Tang et al., 2017),  
86 constant *ET*-radiation radio methods, including the *ET*-top-of-atmosphere  
87 irradiance (Cammalleri et al., 2014), *ET*-extraterrestrial solar irradiance (Ryu et al.,  
88 2012) and *ET* -insolation method (Knipper et al., 2020). These methods vary for the  
89 various climates, and land uses, in almost cases, require calibration when applied to a  
90 different region (Alfieri et al., 2017; Chen & Liu, 2020; Delogu et al., 2012).

91 The most widely used method to convert instantaneous satellite measurements to  
92 daily values is called the evaporation fraction (*EF*) method. The *EF* is defined as the  
93 ratio of *ET* to the available energy flux,  $Q$  which is the sum of *ET* and sensible heat  
94 flux (Brutsaert & Sugita, 1992; Shuttleworth, 1989; Sugita & Brutsaert, 1991). This  
95 method assumes that the *EF* remains constant during the day (Nichols & Cuenca,  
96 1993) and thus the daily latent heat flux (e.g., evaporation) is calculated as the product  
97 of the daily mean available energy  $Q$  and *EF* (Chen & Liu, 2020; Hu et al., 2019).

98 Researchers have, however, shown the *EF* is not constant during the daytime  
99 (Gentine et al., 2007; Liu et al., 2020; Panwar et al., 2020; Sobrino et al., 2007).  
100 Using the instantaneous constant *EF* during the midday as its daily mean value will  
101 underestimate the daily *ET* by 5%-30% (Farah et al., 2004; Van Niel et al., 2011,  
102 2012; Yang et al., 2013). The *EF* depends on several environmental factors including  
103 saturation deficit above the well-mixed layer (Lhomme & Elguero, 1999), the solar  
104 radiation intensity, friction velocity, water availability, relative humidity, cloudiness,  
105 and boundary layer entrainment (Gentine et al., 2011)

106 To avoid underestimating the daily *ET* with the *EF* method, Tang & Li (2017)  
107 introduced a new method to calculate the *ET* based on an extra Penman-Monteith's  
108 expanded form Priestley-Taylor equation. They expressed the *EF* as a function of  
109 ratios of daily and instantaneous measured values of the slope of the saturated vapor  
110 pressure, the psychrometric constant, and a decoupling factor representing the relative  
111 contribution of the radiative and aerodynamic terms to the overall *ET*. Tang & Li  
112 (2017) tested their method in the cropped and irrigated North China Plain using

113 instantaneous satellite measurements and ground-based daily observations. They  
 114 found that the daily  $ET$  calculated by their method was more robust and accurate than  
 115 the constant  $EF$  method.

116 Our objective is to improve daily evaporation accuracy from instantaneous  
 117 satellite measurements by adapting Tang & Li (2017) method for land uses other than  
 118 irrigated cropland. The improved method is tested by comparing the flux tower  
 119 measurements in China with evapotranspiration and several intermediate variables  
 120 calculated with datasets of the Moderate Resolution Imaging Spectroradiometer  
 121 (MODIS) Land Product and China Meteorological Forcing. The intermediate tested  
 122 variables are instantaneous and daily air temperature and net radiation, and the daily  
 123  $EF$ . The MODIS Land Product has a spatial resolution of 0.05 degree and the China  
 124 Meteorological Forcing data has a resolution of 0.1 degrees.

## 125 2. Theory

### 126 2.1 Evaporative fraction

127 Satellites provide only instantaneous data at fixed intervals that can range from  
 128 several times a day to once in several days. To extend the instantaneous data to daily  
 129 values, Nishida et al. (2003) assumed that the instantaneously measured evaporation  
 130 fraction,  $EF^i$  during the satellite overpass around noon time was equal to the daily  
 131 evaporation fraction  $EF^d$ . The  $EF$ , that was originally introduced by Brutsaert &  
 132 Sugita, (1992) for calculation of evaporation in Kansas with weather balloons, is  
 133 defined for both instantaneous and daily measurements as the ratio of latent heat flux  
 134 ( $ET$ ) to available energy flux,  $Q$  ( $W m^{-2}$ ):

$$135 \quad EF = \frac{ET}{Q} \quad (1)$$

136 where  $ET$  is the actual evapotranspiration ( $W m^{-2}$ );  $Q$  is the sum of the latent heat flux  
 137 and sensible heat flux, also called the available energy ( $W m^{-2}$ ). The  
 138 evapotranspiration,  $ET$ , can be calculated as the sum of the transpiration from the  
 139 vegetation and the evaporation from the bare soil surface when the energy transfer  
 140 from the vegetation to the soil surface can be neglected (Nishida et al., 2003), i.e.,

$$ET = f_{veg} ET_{veg} + (1 - f_{veg}) ET_{soil} \quad (2)$$

where the subscript "veg" means full vegetation cover and subscript "soil" indicates the soil exposed to solar radiation (called bare soil);  $ET_{veg}$  is the transpiration from the full vegetation cover ( $W m^{-2}$ ),  $ET_{soil}$  is the evaporation from the soil ( $W m^{-2}$ ),  $f_{veg}$  is the portion of the area with the vegetation cover. The equation and the method for

calculating  $f_{veg}$  is given in Appendix A. The available energy  $Q$  ( $W m^{-2}$ ) is expressed by Nishida et al. (2003) as:

$$Q = f_{veg} Q_{veg} + (1 - f_{veg}) Q_{soil} \quad (3)$$

where  $Q_{veg}$  is the available energy for the vegetation ( $W m^{-2}$ ) and  $Q_{soil}$  is the available energy for bare soil ( $W m^{-2}$ ). Equations 1-3 are valid over any period, including instantaneous and daily times.

The instantaneous evaporation fraction,  $EF^i$  may be found by combining Eqs. 1, 2, and 3 as:

$$EF^i = f_{veg} \frac{Q_{veg}^i}{Q^i} EF_{veg}^i + (1 - f_{veg}) \frac{Q_{soil}^i}{Q^i} EF_{soil}^i \quad (4)$$

where the superscript  $i$  stands for the instantaneous value of the parameter,  $EF_{veg}^i$  and

$EF_{soil}^i$  are the instantaneous evaporation fractions for the vegetation and bare soil,

respectively. Combing the complementary relationship as described by Bouchet (1963), Morton (1978), Brutsaert and Stricker (1979), and Nishida et al. (2003):

$$ET + PET = 2 ET_0 \quad (5)$$

$PET$  is the potential  $ET$  ( $W m^{-2}$ ), described by the Penman-Monteith potential  $ET$  equations,  $ET_0$  is the  $ET$  when  $ET$  equals to the potential  $ET$  ( $W m^{-2}$ ), described by

the Priestley-Taylor equation, the  $EF_{veg}^i$  can be expressed as a function of

instantaneously measured parameters as:

$$EF_{veg}^i = \frac{\alpha \Delta^i}{\Delta^i + \gamma (1 + r_{cveg}^i / 2r_{aveg}^i)} \quad (6)$$

where  $\alpha$  is the Priestley-Taylor parameter which was set to 1.26 (De Bruin, 1983);  $\Delta^i$  is the slope of the saturated vapor pressure, which is a function of the temperature (Pa K<sup>-1</sup>);  $\gamma$  is the psychrometric constant (Pa K<sup>-1</sup>);  $r_{cveg}^i$  is the instantaneous surface resistance of the vegetation canopy (s m<sup>-1</sup>);  $r_{aveg}^i$  is the instantaneous aerodynamics resistance of the vegetation canopy (s m<sup>-1</sup>). Expressions for the surface and the aerodynamic resistances and slope of the saturated vapor pressure can be found in Appendices B and D.

Assuming that the evaporation fraction of bare soil is constant during the day,  $EF_{soil}^i$  was expressed by Nishida et al. (2003) as a function of the instantaneous soil temperature and the available energy based on the energy balance of the bare soil:

$$EF_{soil}^i = \frac{T_{soilmax}^i - T_{soil}^i}{T_{soilmax}^i - T_a^i} \frac{Q_{soil0}^i}{Q_{soil}^i} \quad (7)$$

where  $T_{soilmax}^i$  is the instantaneous maximum possible temperature at the surface reached when the land surface is dry (K),  $T_{soil}^i$  is the instantaneous temperature of the bare soil (K),  $T_a^i$  is the instantaneous air temperature,  $Q_{soil0}^i$  is the instantaneous available energy when  $T_{soil}^i$  is equal to  $T_a^i$  (W m<sup>-2</sup>).

## 2.2 Daily evaporation fraction values based on decoupling parameter

Huang et al. (2017) observed that the Nishida (2003) instantaneous midday evaporative fraction,  $EF^i$  underestimated the daily  $EF^d$ . To correct for the underprediction, Tang & Li (2017) introduced a new expression based on the Penman-

184 Monteith equation and McNaughton-Jarvis equation to calculate the daily  $EF^d$  that is  
185 more generally known as the decoupling factor method:

$$186 \quad EF^d = EF^i \frac{\Delta^d}{\Delta^d + \gamma} \frac{\Delta^i + \gamma}{\Delta^i} \frac{\Omega^{\dot{i}i}}{\Omega^{\dot{i}d}} \frac{\Omega^d}{\Omega^i} \quad (8)$$

187 where superscript "d" means daily; the  $EF^i$  is the midday instantaneous evaporation  
188 fraction;  $\Omega$  is decoupling factor that represents the relative contribution of radiative  
189 and the aerodynamic terms to the overall evapotranspiration (McNaughton & Jarvis,  
190 1983),  $\Omega^{\dot{i}i}$  is the value of the decoupling factor,  $\Omega$ , for wet surfaces. According to  
191 Pereira (2004),  $\Omega$  and  $\Omega^{\dot{i}i}$  can be expressed as:

$$192 \quad \Omega = \frac{1}{1 + \frac{\gamma}{\Delta + \gamma} \frac{r_c}{r_a}} \quad (9)$$

$$193 \quad \Omega^{\dot{i}i} = \frac{1}{1 + \frac{\gamma}{\Delta + \gamma} \frac{r^{\dot{i}i}}{r_a}} \quad (10)$$

$$194 \quad r^{\dot{i}i} = \frac{(\Delta + \gamma) \rho C_p VPD}{\Delta \gamma (R_n - G)} \quad (11)$$

195 where  $r_c$  is the surface resistance (s m<sup>-1</sup>);  $r_a$  is the aerodynamic resistance (s m<sup>-1</sup>);  $r^{\dot{i}i}$   
196 is the critical surface resistance when the actual evapotranspiration equals the  
197 potential evaporation, (called equilibrium evapotranspiration, s m<sup>-1</sup>);  $\rho$  is the air  
198 density (kg m<sup>-3</sup>);  $C_p$  is the specific heat of the air (J kg<sup>-1</sup> K<sup>-1</sup>);  $VPD$  is the vapor  
199 pressure deficit of the air (Pa). The method to calculate the slope of the saturated  
200 vapor pressure  $\Delta$  is specified in Eq. B1; the calculation of vapor deficit,  $VPD$ , from  
201 satellite data is described in Appendix B with Eqs B2- B5. The resistance factors are  
202 further detailed in Appendix D.

203 The decoupling method (Eq. 8) performed well for irrigated cropland (Tang et al.,  
204 2017; Tang & Li, 2017). In this study, we were interested in finding the evaporation of  
205 all landscapes. Thus, we need to adapt Eq. 8 for other land uses such as grassland and  
206 forest. To do this, the constant  $EF_{veg}$  in Eq. 6 and  $EF_{soil}$  in Eq. 7 are reformulated  
207 similarly to the decoupling method in Eq 8:

$$EF_{veg}^d = \frac{\alpha \Delta^i}{\Delta^i + \gamma \left( 1 + \frac{r_{cveg}^i}{2r_{aveg}^i} \right)} \left( \frac{\Delta^d}{\Delta^d + \gamma} \frac{\Delta^i + \gamma}{\Delta^i} \frac{\Omega_{veg}^{i,i}}{\Omega_{veg}^{i,d}} \frac{\Omega_{veg}^d}{\Omega_{veg}^i} \right) \quad (12)$$

$$EF_{soil}^d = \frac{T_{soilmax}^i - T_{soil}^i}{T_{soilmax}^i - T_a^i} \frac{Q_{soil0}^i}{Q_{soil}^i} \left( \frac{\Delta^d}{\Delta^d + \gamma} \frac{\Delta^i + \gamma}{\Delta^i} \frac{\Omega_{soil}^{i,i}}{\Omega_{soil}^{i,d}} \frac{\Omega_{soil}^d}{\Omega_{soil}^i} \right) \quad (13)$$

210 Substituting  $EF_{veg}^d$  (Eq. 12) and  $EF_{soil}^d$  (Eq. 13) into Eq. 4:

$$ET^d = f_{veg} \frac{Q_{veg}^i}{Q^i} EF_{veg}^d + (1 - f_{veg}) \frac{Q_{soil}^i}{Q^i} EF_{soil}^d \quad (14)$$

212 According to Eq. 1, the daily evaporation  $ET^d$  is:

$$ET^d = EF^d Q^d \quad (15)$$

214 In practice, the instantaneous parameter value for calculating  $EF^d$  and  $ET^d$  in Eqs  
 215 12-15 are often not very precise when derived from the available satellite  
 216 measurements. We, therefore, introduced eight approximations to determine the daily  
 217 averaged evaporation fraction  $EF^d$  and evaporation  $ET^d$  and then tested how well  
 218 these approximations could reproduce independently measured  $EF$  and  $ET$  values  
 219 with flux tower data (Table 1). The first method in Table 1, named ETd, computed the  
 220 evaporation with all the daily and instantaneous parameters in Eq. 12 and 13. The  
 221 subsequent methods in Table 1, named ET0-ET7, used various approximations to find  
 222 daily parameters. The second approximation, ET0, in Table 1 is Nishida's method  
 223 (2003, Eq 6). It assumed that the daily values were equal to the instantaneously  
 224 measured values during satellite overpass. Other methods used various ways to  
 225 approximate the daily values. They included the slope of saturated vapor pressure vs.  
 226 air temperature, ET1, the surface resistance, aerodynamic resistance, decoupling  
 227 parameter resistance ET2-ET4, and decoupling factors, ET5 - ET7 (Table 1).

228 **Table 1.** Equations for the complete methods using all instantaneous values. EFd, the  
 229 Nishida (2003) method EF0, and seven approximations EF1-EF7 for calculating the  
 230 daily values  $EF^d$  from the instantaneous evaporation fraction  $EF^i$ , based on Eqs 11-14  
 231 The superscript d indicates a daily value and the superscript i the instantaneous value.

$EF$	Assumption	Equation	$ET$
------	------------	----------	------

<i>EF<sup>d</sup></i>	<i>No assumptions</i>	$EF^d = EF^i \frac{\Delta^d}{\Delta^d + \gamma} \frac{\Delta^i + \gamma}{\Delta^i} \frac{\Omega^{i,i}}{\Omega^{i,d}} \frac{\Omega^d}{\Omega^i}$	<i>ET<sup>d</sup></i>
<i>EF0</i>	$EF^i = EF^d$	$EF0 = EF^i$	<i>ET0</i>
<i>EF1</i>	$\Delta^i = \Delta^d$	$EF1 = EF^i \frac{\Omega^{i,i}}{\Omega^{i,d}} \frac{\Omega^d}{\Omega^i}$	<i>ET1</i>
<i>EF2</i>	$r_c^i = r_c^d$	$EF2 = EF^i \frac{\Delta^d}{\Delta^d + \gamma} \frac{\Delta^i + \gamma}{\Delta^i} \frac{\Omega^{i,i}}{\Omega^{i,d}} \frac{\Omega^d}{\Omega^i}$	<i>ET2</i>
<i>EF3</i>	$r_c^i = r_c^d$	$EF3 = EF^i \frac{\Delta^d}{\Delta^d + \gamma} \frac{\Delta^i + \gamma}{\Delta^i} \frac{\Omega^{i,i}}{\Omega^{i,d}} \frac{\Omega^d}{\Omega^i}$	<i>ET3</i>
<i>EF4</i>	$r^{i,i} = r^{i,d}$	$EF4 = EF^i \frac{\Delta^d}{\Delta^d + \gamma} \frac{\Delta^i + \gamma}{\Delta^i} \frac{\Omega^{i,i}}{\Omega^{i,d}} \frac{\Omega^d}{\Omega^i}$	<i>ET4</i>
<i>EF5</i>	$\Omega^i = \Omega^d$	$EF5 = EF^i \frac{\Delta^d}{\Delta^d + \gamma} \frac{\Delta^i + \gamma}{\Delta^i} \frac{\Omega^{i,i}}{\Omega^{i,d}}$	<i>ET5</i>
<i>EF6</i>	$\Omega^{i,i} = \Omega^{i,d}$	$EF6 = EF^i \frac{\Delta^d}{\Delta^d + \gamma} \frac{\Delta^i + \gamma}{\Delta^i} \frac{\Omega^d}{\Omega^i}$	<i>ET6</i>
<i>EF7</i>	$\frac{\Omega^{i,i}}{\Omega^{i,d}} \frac{\Omega^d}{\Omega^i} = 1$	$EF7 = EF^i \frac{\Delta^d}{\Delta^d + \gamma} \frac{\Delta^i + \gamma}{\Delta^i}$	<i>ET7</i>

---

### 232 3 Material, methods and data

233 This section presents the data and the methods used in calculating the satellite-  
234 based daily evaporation fraction,  $EF^d$  and the daily evaporation  $ET^d$ , using Eqs 11-14  
235 with and without the simplifying approximations listed in Table 1. A description of the  
236 data available for seven flux towers in China closes this section (Table 2). Note that  
237 the MODIS satellite data are available for 250 m, 500 m, and 0.05 degree  
238 (approximately 5 km) grids. While the smallest grid size would likely be more  
239 representative of the grid tower measurements used for validation, we chose to use the  
240 larger size because we intended to develop a method for large areas such as China.  
241 Even with the computer capabilities, using the two smallest grids as input would  
242 result in excessive amounts of data and computer time. For that reason, we chose the  
243 0.05-degree grid data as input.

#### 244 3.1 Data used for calculating satellite-based daily $EF$ and $ET$

245 The schematic to calculate the evaporation fraction,  $EF$  (Eq. 14), and the  
246 evaporation  $ET$  (Eq. 15) is shown in Figure 1. The input consists of the MODIS  
247 Land Product and China Meteorological Forcing datasets (Table 2).

248 The MODIS data for China were downloaded for 2001 to 2018 from the website  
249 <https://modis.gsfc.nasa.gov/>. The input data consisted of the following instantaneously  
250 measured data each day around noon (Figure 1, Table 2a): the surface reflectance  
251 (MOD09CMG), surface temperature/emissivity (MOD11C1), albedo (MCD43C3),  
252 16-day NDVI (MOD13C1), and yearly land cover classes compiled from MODIS  
253 data by the International Geosphere-Biosphere Programme, IGBP (MCD12C1). In  
254 addition, the China Meteorological Forcing solar radiation dataset was downloaded  
255 from <http://data.tpdc.ac.cn/en/data/> (Table 2). The solar radiation had a resolution of  
256 0.1 degree and a 3-hour time step and was described in detail in (He et al., 2020; Yang  
257 et al., 2006, 2010) and Huang et al. (2017).

258

259 **Table 2a** Input data used in this study

Input data (2001-2018)				
Data source	Data name	Used parameter	Time step	Spatial resolution
<b>MODIS Land Product</b>	MOD11C1	Land Surface Temperature	daily	0.05 degree
<a href="http://data.tpdc.ac.cn/en/data/">http://data.tpdc.ac.cn/en/data/</a>	MOD09CMG	Surface Reflectance	daily	0.05 degree
	MCD43C3	Albedo	daily	0.05 degree
	MOD13C1	NDVI	16-day	0.05 degree
	MCD12C1	Land cover	yearly	0.05 degree
<b>China Meteorological Forcing</b>	Srad	shortwave radiation	3-hourly	0.1degree
<b>Dataset</b>				
<a href="https://modis.gsfc.nasa.gov/data/">https://modis.gsfc.nasa.gov/data/</a>				

260 **Table 2b** Data for verification

Flux tower	Lon. (°E)	Lat. (°N)	Altitude (m)	Land cover	Footprint (m)	Climate	Time period
Changbaishan	128.1	42.4	738	Forest	181 to 3070	Monsoon temperate continental climate	2003-2005
Qianyanzhou	115.06	26.74	102	Forest	120 to 1655	Subtropical monsoon climate	2003-2005
Dinghushan	112.53	23.17	240	Forest	129 to 1908	Monsoon humid climate	2003-2005
Yucheng	116.57	36.83	28	Cropland	16 to 190	Semi-humid monsoon climate	2003-2005
Haibei	101.32	37.62	3190	Grassland	19 to 195	Plateau continental climate	2003-2005
Neimeng	116.67	43.53	1200	Grassland	19 to 195	Temperate arid and semiarid continental climate	2004-2005
Dangxiong	91.07	30.5	4350	Grassland	27 to 163	Plateau monsoon climate	2004-2005
Wujiaqu	87.67	44.41	438	Grassland	400	Temperate arid and semiarid continental climate	2020.2.7- 2020.12.17

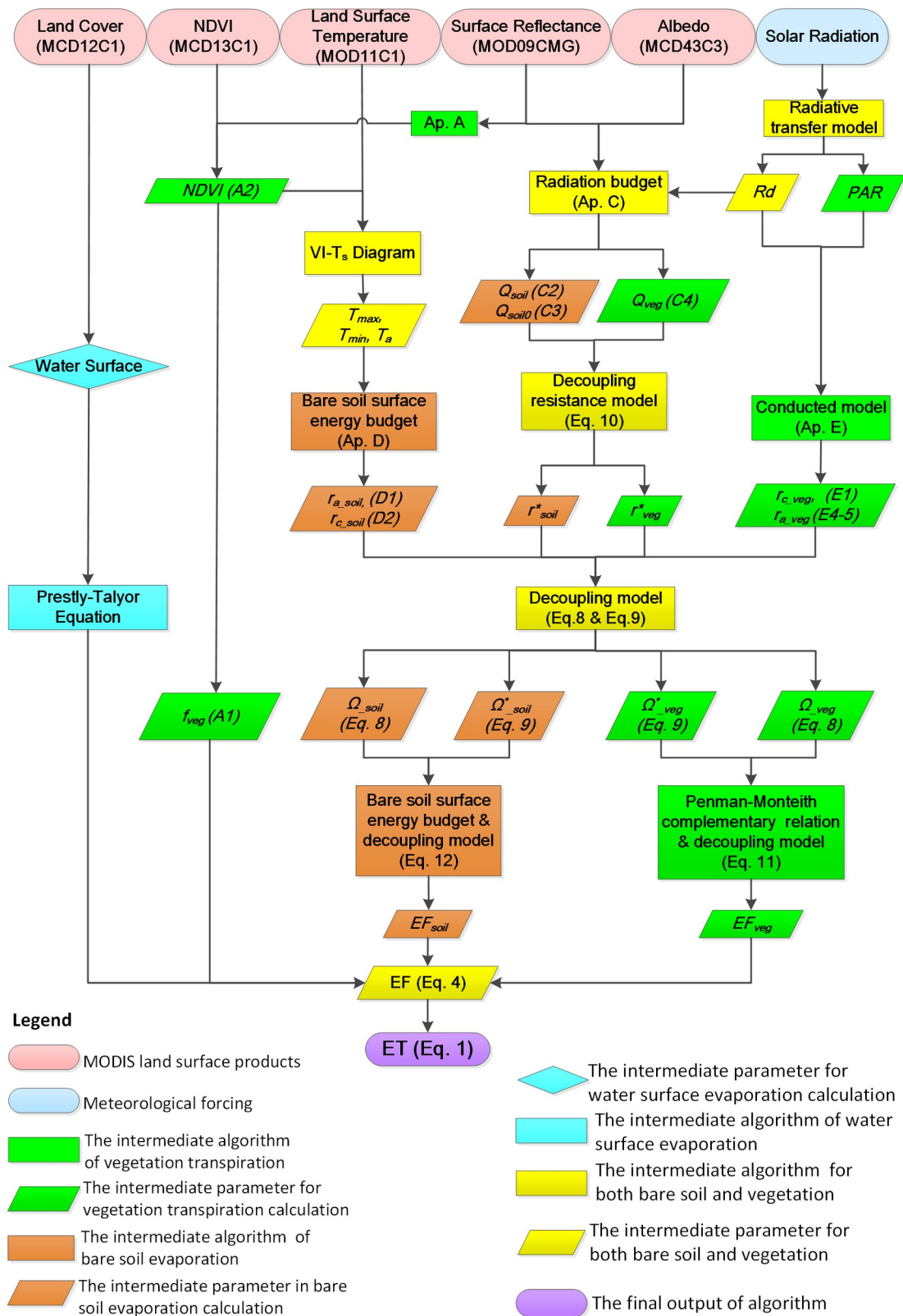
261 3.2 Procedures for calculating satellite-based daily  $EF$  and  $ET$ 

262 Figure 1 shows how to obtain the variable values to calculate the  $EF$  using the  
263 data described in section 3.1. The vegetation fraction,  $f_{veg}$  (Eq 13) was calculated with  
264 Eq. A1 in Appendix A based on the Normalized Difference Vegetation Index, NDVI,  
265 derived from the reflectance data in the MOD09CMG product (Eq. A2). When the  
266 daily reflectance data was not available, the MOD13C1 (measuring NDVI with a 16-  
267 day interval) was used as an auxiliary data source (Nishida et al., 2003). The actual  
268 available energy for the bare soil surface,  $Q_{soil}$  (Eq 13), was calculated by the radiation  
269 energy budget with the data of the MOD11C1 product using Eqs C1-C3 in Appendix  
270 C (Figure 1). The available energy for the vegetation  $Q_{veg}$  (Eq 13), was obtained by  
271 using the air temperature with Eq. C3 in Appendix C. The air temperature was

272 determined in Appendix F with the Nishada's Vegetation Index – temperature, VI-T<sub>s</sub>  
273 diagram using the NDVI (MOD09CMG and MOD13C1), and the surface temperature  
274 tabulated in the MOD11C1 product with the diagram. The VI-T<sub>s</sub> diagram was based  
275 on the assumption that dense vegetation has the minimum surface temperature and  
276 that dry, bare soil has the maximum temperature. Thus, there is a negative correlation  
277 between vegetation coverage and surface temperature. The calculation of the slope of  
278 the vegetation coverage, the surface temperature (also called the warm edge), and the  
279 intercept of them (also called the minimum surface temperature) is shown in  
280 Appendix F.

281 The instantaneous and daily equations were of the same form (Appendices D and  
282 E). The aerodynamic resistance of the bare soil,  $r_{a\ soil}$  was determined with the  
283 equation D1 in appendix D originally proposed by Nishida (2003). The surface  
284 resistance of the bare soil,  $r_{c\ soil}$  was found by subtracting the aerodynamic resistance  
285 of the bare soil from the total aerodynamic resistance (Eq. D2). The total aerodynamic  
286 resistance was computed with Eq. D3 (Griend and Owe, 1994 and Mu, 2007). The  
287 canopy surface resistance,  $r_{c\ veg}$  was obtained with the method developed by Jarvis  
288 (1976, Eq. E1-E3 in Appendix E). The aerodynamic resistance of the forest cover was  
289 obtained with Eq. E4 and of both grassland and cropland with Eq. E5 (Kondo, 2000).  
290 The wind speed, which was input in Eqs E4 and E5, is given in Eq E6-E8. Then, the  
291 instantaneous and daily surface and aerodynamic resistance were computed with the  
292 equations provided in Appendices D and E using a combination of all available  
293 MODIS and Meteorological products as shown in Figure 1. Finally, these resistances  
294 were used to calculate the  $EF_{veg}$  in Eq. 5 and  $EF_{soil}$  in Eq. 6

295



296

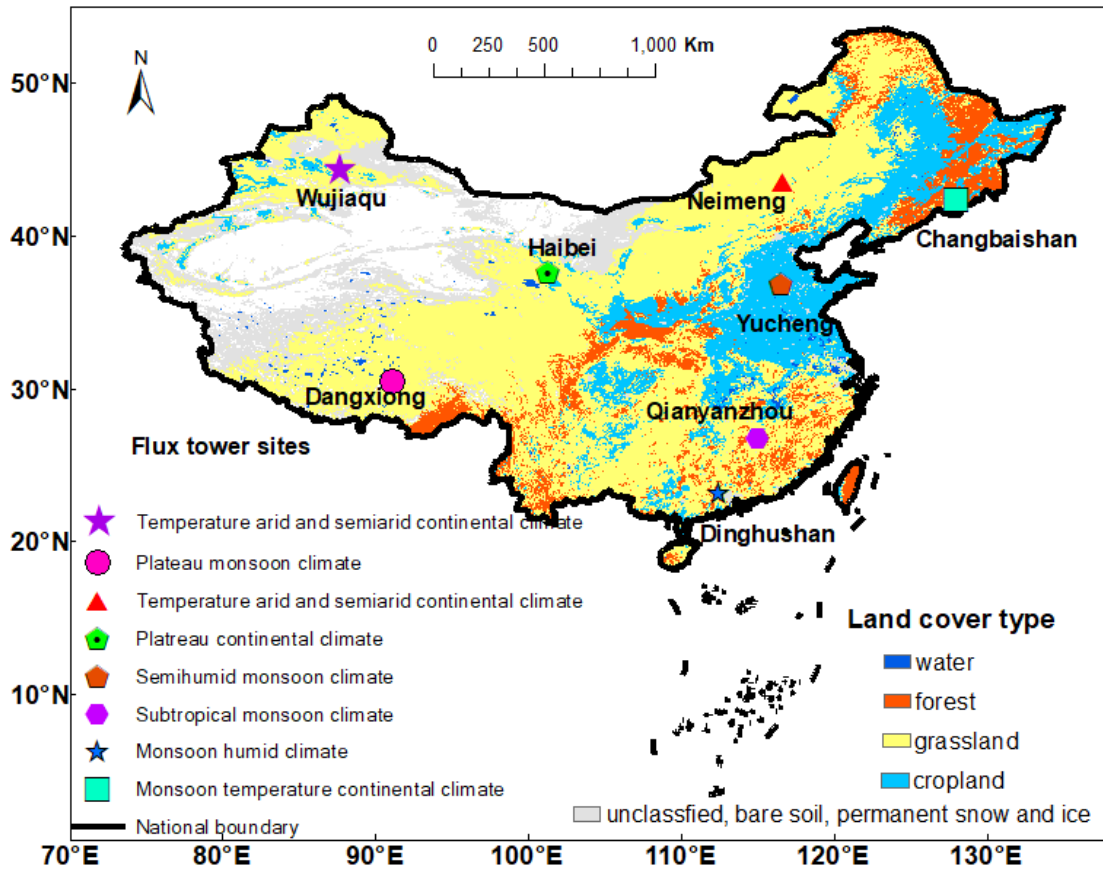
297 **Figure 1:** Schematic to calculate the evaporation fraction,  $EF$  (Eq. 13) and  
 298 evaporation (Eq. 14). The ovals in the top row are the databases, and the square boxes  
 299 are the algorithms, and parallelograms are the parameters. The numbers in the  
 300 parenthesis are the equation to determine the parameters.

### 3.3 Data used for ground-truthing $EF$ , $ET$ and its components

The validity of the methods in Table 1 for calculating the actual  $ET$  was examined with data from seven flux towers from the Chinese FLUX Observation and Research Network (ChinaFlux): ChangBaiShan (CBS), QianYanZhou (QYZ), DingHuShan (DHS), YuCheng (YC), Haibei (HB), Neimeng (NM) and Dangxiong (DX) (Yu et al., 2006, 2008, 2013). These 7 flux towers are situated throughout China in different climate zones. CBS is in the monsoon temperate continental climate; QYZ and DHS are in the humid monsoon climate; YC is in the monsoon semi-humid climate; NM is in the temperate arid and semiarid continental climate; HB and DX sites are in the plateau continental climate, and land use, including forest, alpine, and grassland, as shown in Figure 2. The period considered was from 2003 to 2005 for CBS, QYZ, DHS, YC, and HB, and from 2004 to 2005 for the NM and DX sites. The sensible heat flux, latent heat flux, air temperature, and solar radiation observations are measured with a sampling frequency of 10 Hz with the open-path eddy covariance (3-D Sonic Anemometer of Campbell, and Li7500CO<sub>2</sub>/H<sub>2</sub>O analyzer of LI-COR) and standard meteorology equipment observations are aggregated every 30 minutes. The solar radiation, air temperature, and latent heat flux data at the closest 30-minute time interval to the MODIS Terra overpass time were used for instantaneous time scale validation. Daily temperatures were the average of the half-hour temperatures from 6:00 to 18:00. The Wujiaqu site is in the temperate arid and semiarid continental climate, and the measurement period was from Feb.7, 2020 to Dec. 17, 2020. The albedo measurements in the Wujiaqu site were used for diurnal albedo ground-truthing.

Several factors can cause discrepancies between satellite predicted  $EF$  and  $ET$  and flux tower measurements. These discrepancies may be due to the mismatch in the flux tower and the satellite footprint, the unsuitability of the satellite methods to the environmental conditions at the flux tower site (specifically high altitude sites with frozen soils and deserts), inaccuracies in the underlying assumptions of the theory, etc. We assumed the underlying assumptions were at fault when there was a

330 consistent difference for most flux towers. When the mismatch between our estimates  
 331 and the flux tower measurements was for only a few of the flux towers, environmental  
 332 factors and the particular site's footprint were likely the cause.  
 333



335 **Figure 2.** The location of the seven flux tower sites of the FLUX Observation and  
 336 Research Network (ChinaFlux): ChangBaiShan (CBS), QianYanZhou (QYZ),  
 337 DingHuShan (DHS), YuCheng (YC), HaiBei (HB), Neimeng (NM), WuJiangQu  
 338 (WJQ) and Dangxiong (DX). The 5 land cover types include water, forest, grassland,  
 339 cropland, unclassified, bare soil, permanent snow, and ice, are shown in Figure 2.

#### 340 3.4 Statistical methods

341 To compare the daily satellite evaporation ( $ET_{MOD}^d$ ) calculation with the flux  
 342 tower observed  $ET_{Obs}^d$ , the Pearson's correlation coefficient ( $r$ ) and Root Mean Square  
 343 Error (RMSE) were calculated.

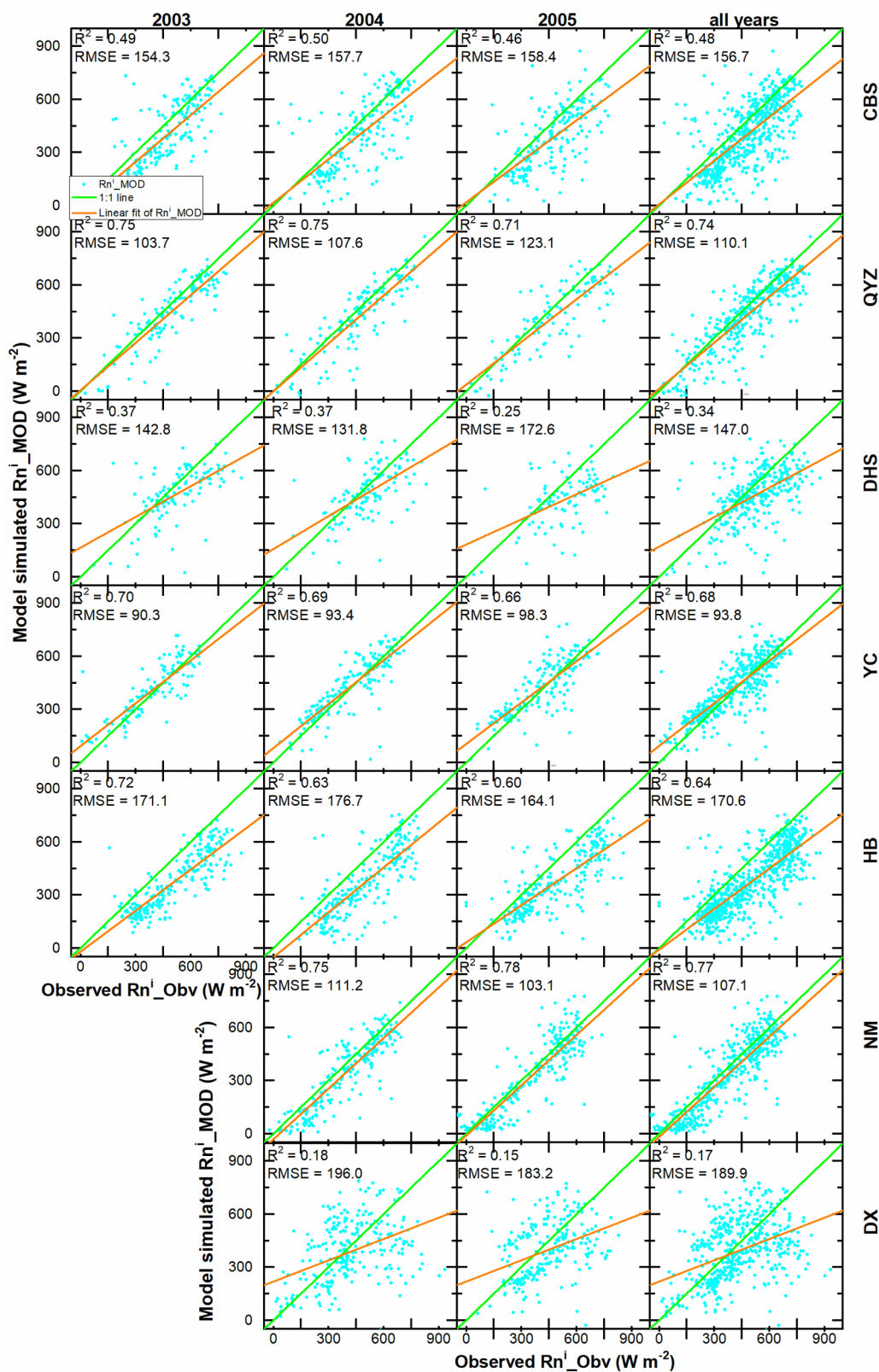


367 shortwave radiation ranged from 0.77 to 0.92, and RMSE varied between 27.1 and  
368  $40.4 \text{ W m}^{-1}$  (Figure H2 in Appendix H). The discrepancy between the two  
369 measurement techniques was the largest for the Dinghushan(DHS), Haibei(HB), and  
370 Dangxiong(DX) sites. The observed incoming shortwave radiation for the DHS site  
371 located in southeast China with a monsoon climate was greater than that of the CMFD  
372 because the albedo was overestimated during the rainy phase (Huang et al., 2017).  
373 The HB and DX sites are both situated at high elevations. According to Yang et al.  
374 (2006), shortwave radiation was underestimated.

## 375 4.2 Net radiation

### 376 4.2.1 Instantaneously net radiation

377 The satellite-based model simulated instantaneous net radiation  $Rn_{MOD}^i$  was  
378 calculated by Eq C1 and C2 in Appendix C. In Figure 3,  $R_c^i$  shows a good agreement  
379 with the instantaneous net radiation for four of the seven flux towers at the time of the  
380 satellite overpass. This is consistent with the generally good fit of the instantaneous  
381 incoming shortwave radiation (Appendix H1). Although  $Rn_{MOD}^i$  are consistently  
382 underestimated in the CBS, QYZ, YCand NM four sites, it has satisfactory regression  
383 coefficients,  $R^2$ , ranging from 0.25 to 0.75, and root mean square error (RMSE) from  
384  $90.3 \text{ W m}^{-2}$  to  $158.4 \text{ W m}^{-2}$  (Figure 3). Three remaining three sites (DHS, DX, and  
385 HB) perform poorly with RMSEs ranging from 103.1 to  $198.9 \text{ W m}^{-2}$ . The main reas  
386 on for the weak performance of these three sites are the inadequate quality of the  
387 downloaded incoming shortwave radiation in the CMFD data base (section 4.1,  
388 Appendix H1 and H2)



Fig

389

390 re 3. Scatter plots of satellite based model simulated instantaneous (during MODIS

391 Terra overpass) net radiation  $Rn^i_{MOD}$  against flux tower observed instantaneous air

392 temperature ( $Rn^i_{Obv}$ ) in an individual year and entire period of 2003 to 2005 at

393 Changbaishan (CBS), Qianyanzhou (QYZ), Dinghushan (DHS), Yucheng (YC),  
 394 Haibei (HB), Neimeng (NM) and Dangxiong (DX) sites.

#### 395 4.2.2 Daily net radiation

396 The daily net radiation  $Rn_{MOD}^d$ , calculated by the equation C3 in the Appendix by

397 assuming the longwave outgoing radiation term  $\varepsilon\sigma T_s^4$  equals to the

398  $\varepsilon\sigma T_a^4 + 4\varepsilon\sigma T_a^3(T_s - T_a)$  in Eq. C1.  $Rn_{MOD}^d$  is consistently overestimated the observed

399 net radiation of the seven flux towers as shown in Figure 4, similar to that found by

400 Tang et al. (2009) employed the same algorithms. Despite that the  $R^2$  for most flux

401 sites is good ( $R^2$  ranges from 0.68 to 0.81) but the intercept with the y-axis is positive

402 indicating a systematic error in the calculations. The daily net radiation for QYZ and

403 DHS sites located in the south and southeast China (Figure 4) with a wet and warm

404 climate with dense plant cover is relatively close. The daily net radiation for the other

405 five sites (located in northern China, in colder, more arid, or semiarid climate) with

406 less dense vegetation have a greater offset from the observed values. Especially, the

407 DX site has the poorest fit  $R^2$  of 0.29. We first hypothesized that the systematic error

408 causing the overestimation of the calculated satellite the net energy was related in part

409 to the vegetation density through the longwave radiation term in Eq C1 in appendix C.

410 Because we assumed that for daily scale, the longwave outgoing radiation term

411  $\varepsilon\sigma T_s^4 \approx \varepsilon\sigma T_a^4 + 4\varepsilon\sigma T_a^3(T_s - T_a)$  (Appendix C3), but we compared the  $\varepsilon\sigma T_s^4$  and

412  $\varepsilon\sigma T_a^4 + 4\varepsilon\sigma T_a^3(T_s - T_a)$ , and found they are very close (the difference is lower than

413 1%). Then, we found that assuming the instantaneous albedo as its daily value may be

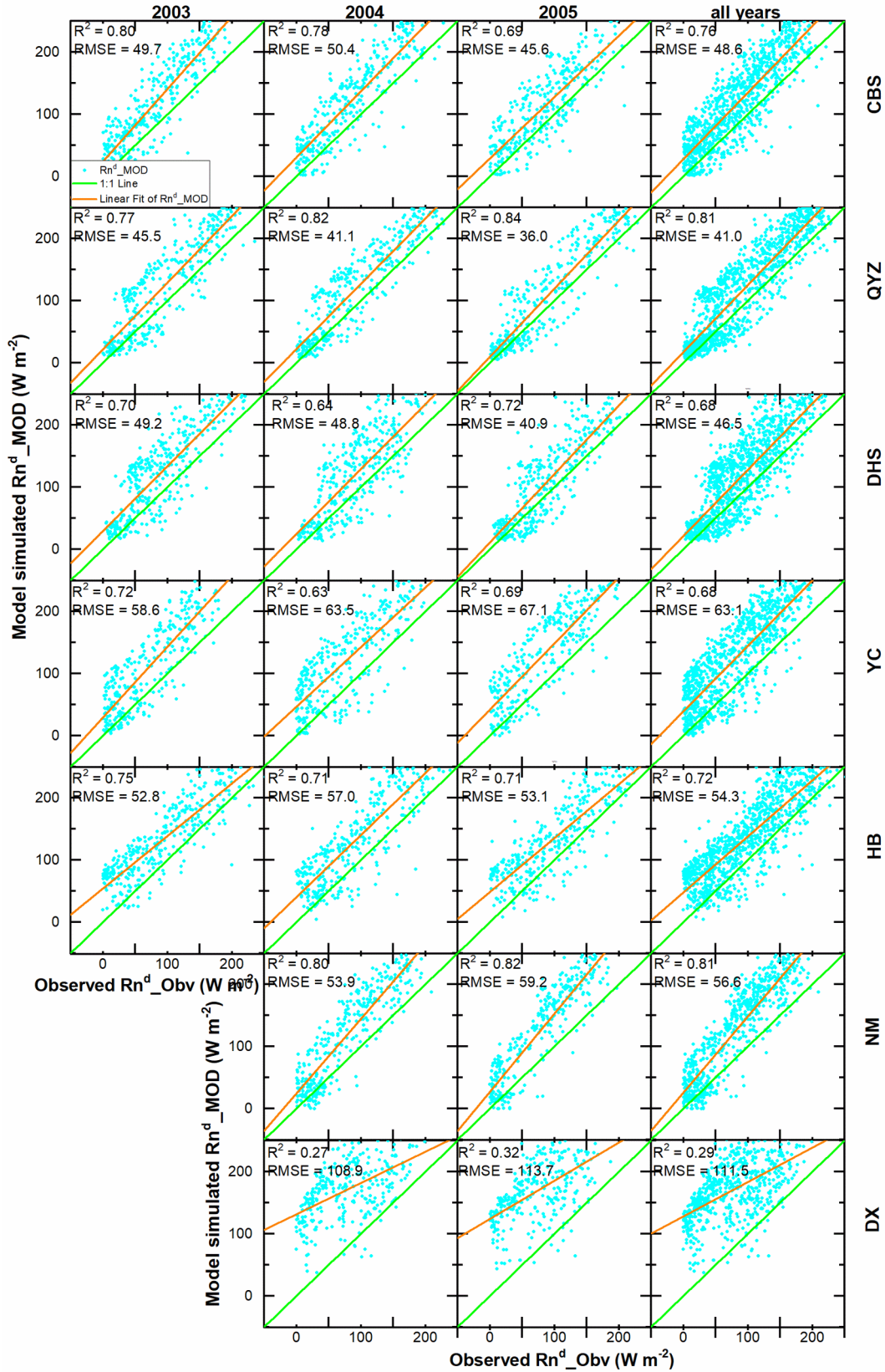
414 the main reason. Studies (Cierniewski et al., 2015; Jääskeläinen & Manninen, 2021;

415 Wang et al., 2015; Zhang et al., 2020) have shown that the albedo has a distinct

416 diurnal variation and it has the minimum values during the noon time during the

417 satellite overpass. Grant et al. found that the instantaneous albedo for a grass cover in

418 Australia was about 30% lower at noon than at 7 AM or 5 PM (Grant et al., 2000) as  
419 the diurnal albedo measurements of Wujiaqu site in Appendix I.



420

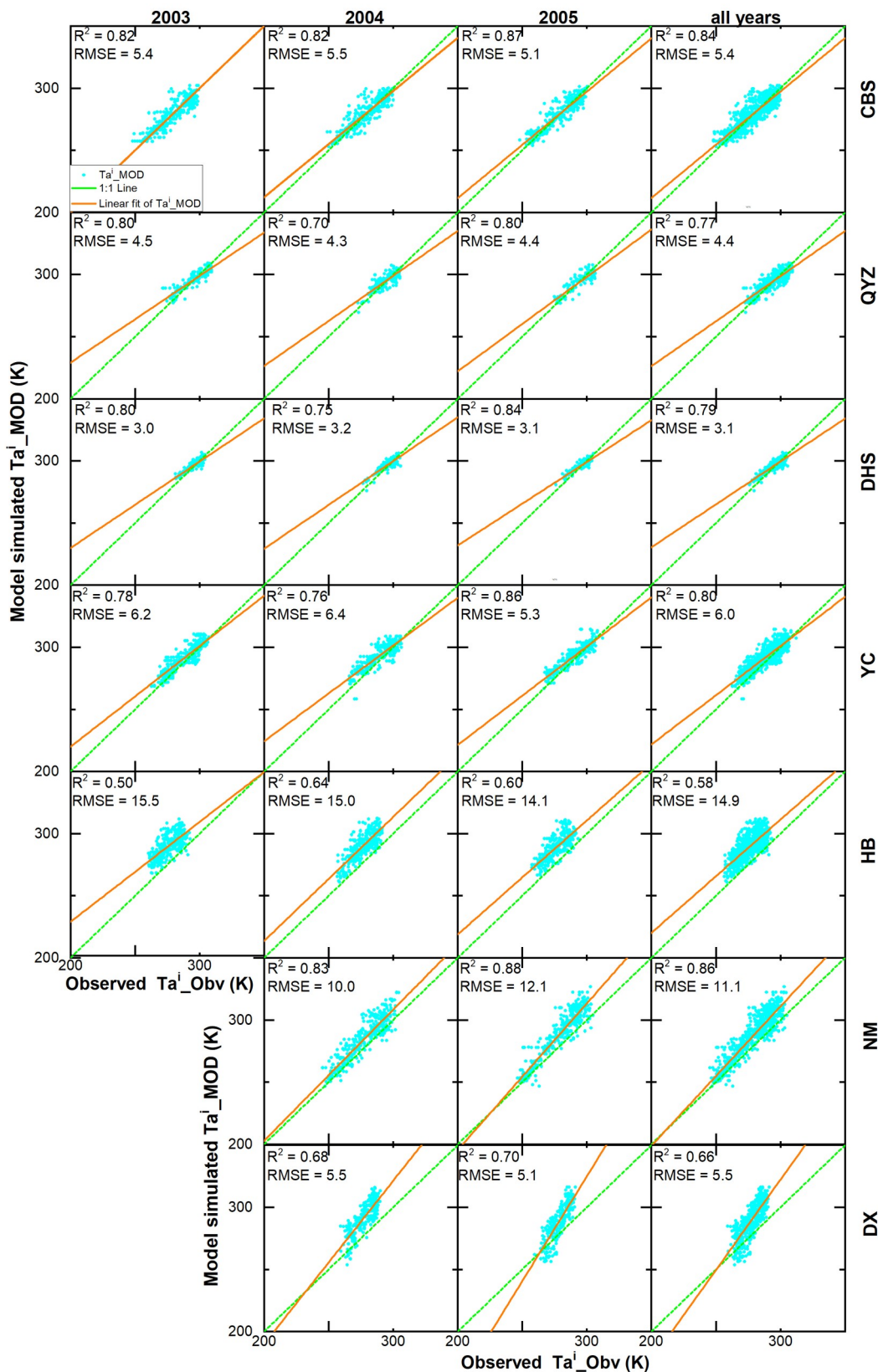
Fig

421 **Figure 4.** Scatter plots of satellite-based model simulated daily net radiation ( $Rn_{MOD}^d$ )  
 422 calculated with Eq. C1 plotted against the observed flux tower measurements ( $Rn^d$   
 423 \_Obv) for an individual year and the entire 2003 to 2005 period. The abbreviation for  
 424 the flux tower sites are in Figure 3, and the locations in Figure 1.

#### 425 4.3 Air temperature

##### 426 4.3.1 Instantaneous air temperature

427 Instantaneous air temperature  $T_{\zeta}^i$  was calculated by the MODIS land surface data  
 428 and NDVI data combined with the VI-Ts method in Appendix F. The comparison of  
 429 the satellite-based instantaneous daytime air temperatures,  $T_{\zeta}^i$  with the observed  
 430 temperature  $T_{\zeta}^i$  at the seven flux towers during the satellite overpass is shown in  
 431 Figure 5. The predicted air temperature is in general agreement with the flux tower  
 432 measurements with  $R^2$  ranging from 0.50 to 0.84 and root mean square (RMSE) from  
 433 3.0 K to 15.9 K. The three sites Haibei, (HB), Neimeng (NM), and Dangxiong (DX)  
 434 that are located at high elevations with an annual average of 0 °C and grass ground  
 435 cover, deviated most (i.e., low  $R^2$  and large RMSE). For these sites at high elevations,  
 436 a distinct relationship between the NDVI and air temperature does not exist when the  
 437 grass is frozen or snow-covered. Hence the underlying assumptions of the VI diagram  
 438 (Appendix F) are violated and resulted in poor estimates of air temperature, as shown  
 439 in Figure 5. When the NDVI has large spatial differences (e.g., forests in northeast  
 440 China at the Changbaishan (CBS) site and cropland in North China Plain at the  
 441 Yucheng (YC) site), the air temperature calculated with the VI-T<sub>s</sub> diagram is  
 442 comparable to the flux tower (Figure 5).



443

444 **Figure 5.** Scatter plots of satellite based model simulated instantaneous (during

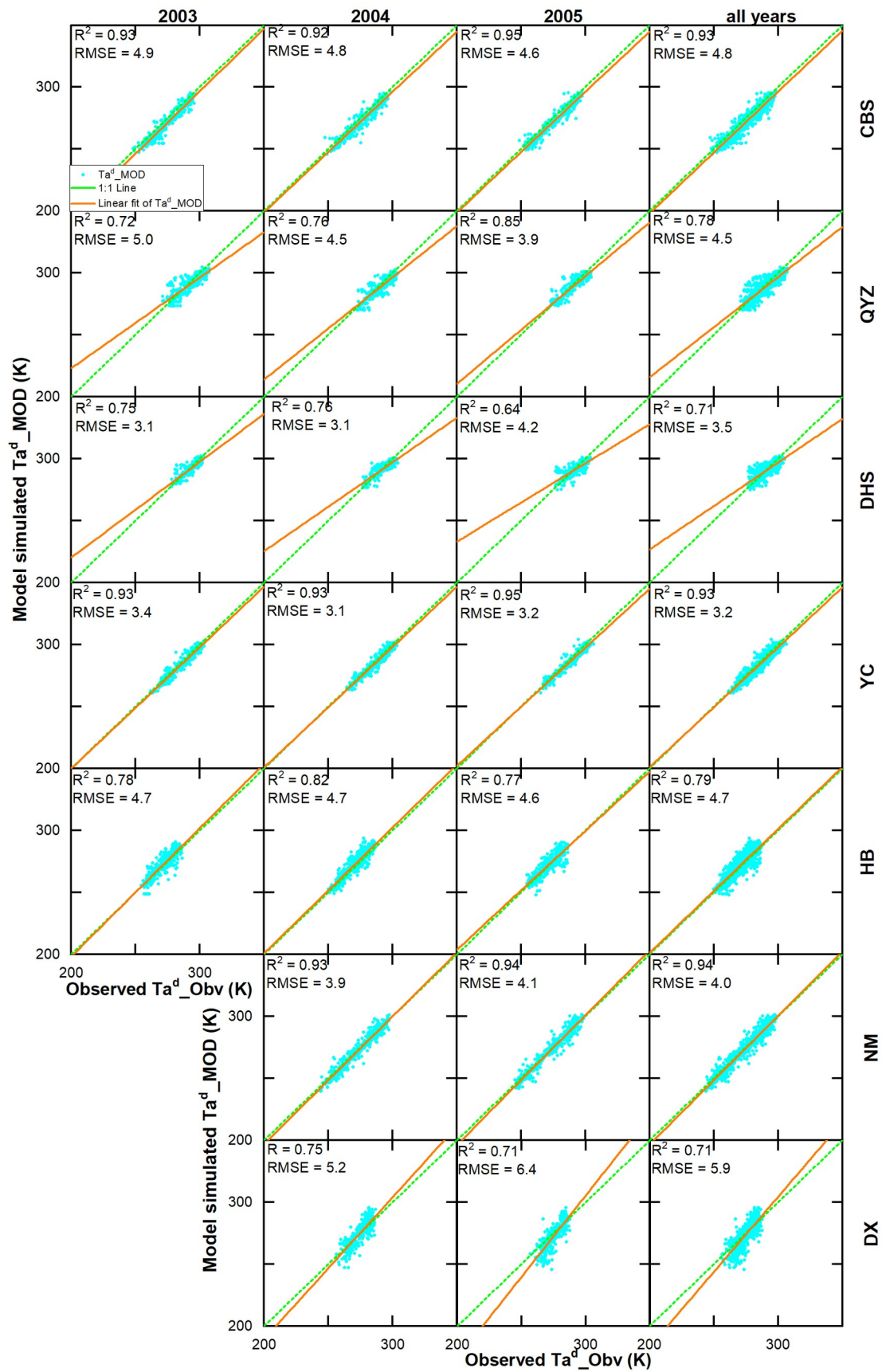
445 MODIS Terra overpass) air temperature  $Ta^i_{MOD}$  against flux tower observed

446 instantaneous air temperature ( $Ta^i_{Obv}$ ) in an individual year and entire period of 2003 to

447 2005. The flux tower abbreviations are in Figure 3, and the locations in Figure 1.

#### 448 4.3.2 Daily air temperature

449 The model simulated daily mean air temperature,  $T_{\text{a}}^{\text{d}}$  was calculated by extending  
450 the daytime and nighttime instantaneous air temperature with a sine and cosine  
451 method in Appendix G.  $T_{\text{a}}^{\text{d}}$  was compared with the daily averaged air temperatures  
452 seven flux towers observations  $T_{\text{a}}^{\text{d}}$  in Figure 6. In general, the fit of the daily  
453 temperatures in Figure 6 is either equal or better than the instantaneous temperatures  
454 in Figure 5, with the  $R^2$  ranging from 0.64 to 0.95 and RMSE ranging from 3.1 K to  
455 6.4 K. Especially for the DX, NM, and HB sites, the fit is much better because 1) the  
456 random biases of flux tower measurements were reduced for the daily scale; 2) the  
457 calculation of the daily air temperature involved the night air temperature that was  
458 calculated by setting the satellite measured land surface temperature equal to the air  
459 temperature and did not involve the problems encountered with the VI-Ts diagram for  
460 these three sites (Appendix F). For the remaining four sites, the daily air temperatures  
461 based on the satellite measurements slightly underestimate the flux tower  
462 measurement (Figure 6). Therefore, the RMSE do not improve significantly over the  
463 instantaneous air temperatures in Figure 5.



464 **Figure 6.** Scatter plots of satellite-based model simulated daily air temperature  $T_a^d$   
 465 against flux tower observed instantaneous air temperature ( $T_a^d$ ) in an individual year  
 466 and entire period. Figures 1 and 3 give the location and abbreviations.

#### 4.4 Evaporation fraction ( $EF$ )

467 The satellite-based evaporative fraction ( $EF$ ) using the approximations in Table  
 468 1 for Eqs 12-15 was averaged over the observation period (Figure 7). As expected, the  
 469 greatest daily evaporation fractions are observed for the QYZ, DHS, and YC sites  
 470 which either have the highest rainfall or are irrigated and thus have ample water to  
 471 satisfy the evaporative demand (Figure 7). The other sites have limited rainfall, and  
 472 thus evaporation is less than the potential evaporation and consequently greater  
 473 amounts of incoming solar radiation converted into sensible heat. The calculated  $EF$   
 474 values for the Dangxiong (DX) site in southwest China for all approximations in  
 475 Table 1 are much lower than the observed  $EF$  values (Table 3). The main reason is  
 476 the difference in vegetative cover for the flux tower's footprint and the grid cell on  
 477 which the satellite measurements. Sixty-five percent is vegetated in the flux tower  
 478 footprint, but only 13 % of the grid cell had vegetation. The DX site will therefore not  
 479 be considered further. The remaining  $EF$  values for the 6 flux tower sites are  
 480 averaged in Table 3.

482 The expressions of daily evaporation fractions in Table 1 can be divided into the  
 483  $EF^d$  method and the remaining methods consisting of  $EF^0$ - $EF^7$ . For  $EF^d$ , all daily  
 484 parameter and instantaneously parameter values were calculated, and for  $EF^0$ - $EF^7$ ,  
 485 one or more of the daily parameters were substituted for the instantaneous parameter  
 486 values. As can be seen in Table 3, when no substitutions were made, the daily  
 487 evaporation fraction,  $EF^d$  for the  $EF^d$  method resulted in a 50% underprediction of  
 488 the observed flux tower  $EF^d$  of 45%. The second group in which substitutions were  
 489 made of instantaneous values for daily parameters,  $EF^0$ , in which the daily  $EF^d$   
 490 equaled to the instantaneous  $EF^i$  during satellite overpass, performs relatively well  
 491 and provides a better estimate for the observed flux tower value than the  $EF^d$ . For  
 492  $EF^1$  in Table 3, the slope of the saturated vapor pressure for the day  $\Delta^d$  was set equal  
 493 to the instantaneous value. The average value of  $EF^1$  for  $EF^d = 0.23$  and is similar to  
 494 the  $EF^d$ , which is half of the observed value. Next is the set of  $EF^2$ - $EF^4$  in which the

495 daily aerodynamic, surface and decoupling parameter resistances were replaced by  
 496 their instantaneous values. None of the three approximation predict the observed  $EF^d$   
 497 very well (Table 3). Finally, the last set consists of EF5-EF7, in which the daily  
 498 decoupling parameters were equated with the instantaneous values. Interestingly the  
 499  $EF^d$  values vary widely in this group and have the lowest performance for EF 5 with  
 500 and an average value of  $EF^d=0.17$  and the best performance for EF6 with  $EF^d=0.41$ .  
 501 The latter is closer to the observed value of 0.45 than any other approximations,  
 502 including the original method (EF0) proposed by Nishida and EFd that uses the  
 503 complete equation (Eqs 11-14) without substitution Table 3.

504 The EF6 (as well as EF0 and EF7) method predicted the observed value  $EF^d$   
 505 value most accurately because in all the three methods the  $\Omega^{i,d}$  was replaced by the  
 506 instantaneous value  $\Omega^{i,i}$  in some form (as can be seen from Table 1). Both  $\Omega^{i,d}$  and  $\Omega^{i,i}$   
 507 were calculated with Eq.10 in which either daily or instantaneous values were used of  
 508 the following independent parameters: the slope of the saturated vapor pressure, the  
 509 psychrometric constant, the aerodynamic resistance and  $r^{\zeta}$ . Considering these four  
 510 independent parameters in Eq 10, we note that critical surface resistance  $r^{\zeta}$  in Eq 11 is  
 511 a function of the net radiation. As shown in Figure 4, the instantaneous net radiation is  
 512 predicted much more accurately than the daily net radiation in Figure 5, which is  
 513 overestimated by 20-40% using MODIS parameters. It means since the net radiation  
 514 is the denominator in Eq 11, the instantaneous critical surface resistance  $r^{\zeta,i}$  is  
 515 estimated relatively well, while the daily critical surface resistance  $r^{\zeta,d}$  is too small. In

516 turn, this calculates  $\Omega^{i,i}$  correctly and gives a too large  $\Omega^{i,d}$ , thus, the  $\frac{\Omega_i^{\zeta}}{\Omega_d^{\zeta}}$  is too small.

517 In the calculation of the daily evaporation fraction,  $EF^d$ , in Eq 9, the  $\frac{\Omega_i^{\zeta}}{\Omega_d^{\zeta}}$  term is in the  
 518 denominator, and hence the  $EF^d$  is underestimated for all approximations (i.e., EF1-

82

519 EF5) that use the calculated  $\frac{\Omega_i^c}{\Omega_d^c}$  value.

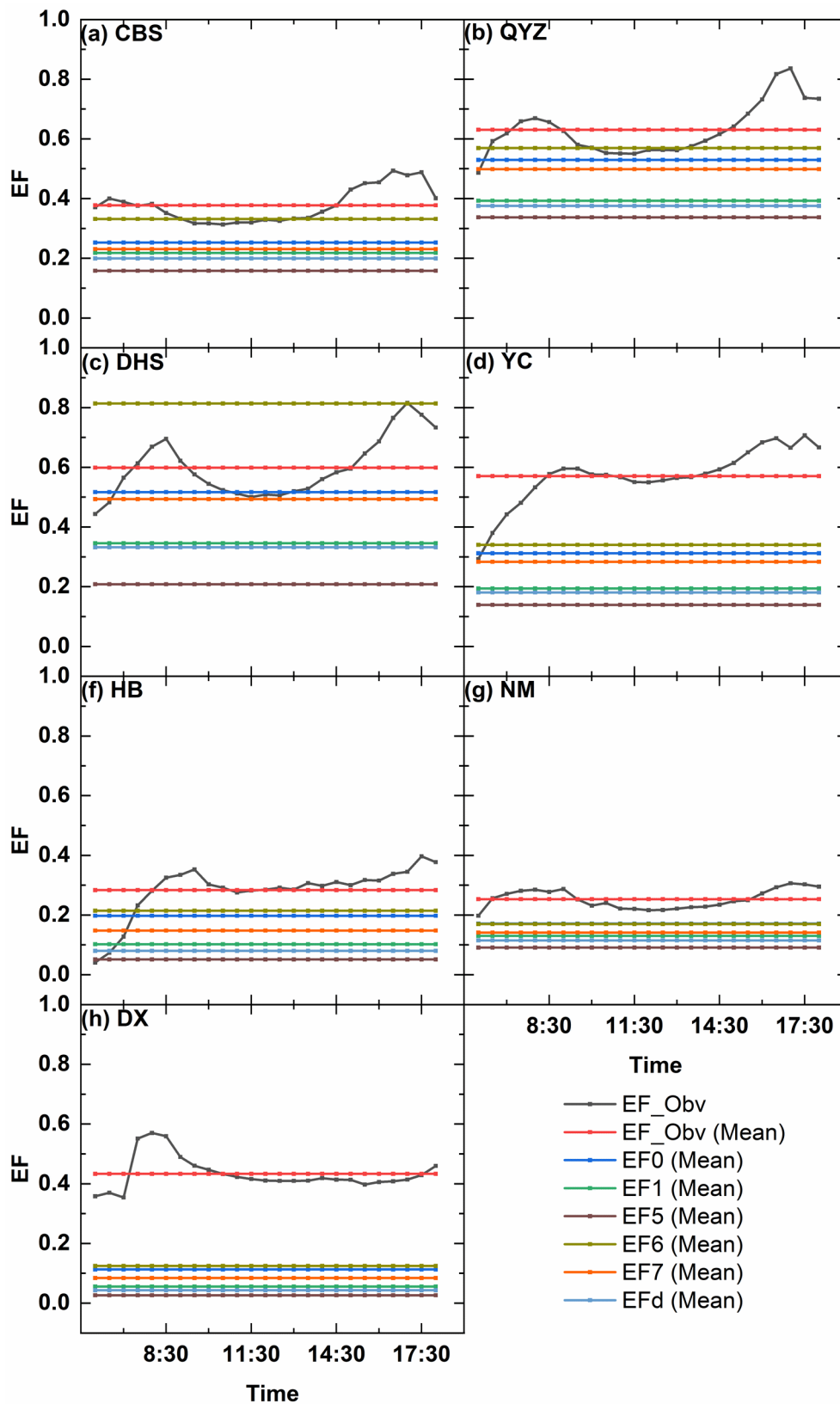
520

521

522 **Table 3.** The comparison of the flux tower observed daily mean evaporative fraction  
 523 ( $EF_{Obs}$ ) and the satellite-based estimated  $EF$  with various methods (ET0-ET7  
 524 and ETd) during 2003 to 2005 at Changbaishan (CBS), Qianyanzhou (QYZ),  
 525 Dinghushan (DHS), Yucheng (YC), Haibei (HB), Neimeng (NM) and Dangxiong  
 526 (DX) sites.

<b>Site</b>	<b>Observed</b>	<b>EF0</b>	<b>EF1</b>	<b>EF2</b>	<b>EF3</b>	<b>EF4</b>	<b>EF5</b>	<b>EF6</b>	<b>EF7</b>	<b>EFd</b>
<b>CBS</b>	0.38	0.25	0.22	0.22	0.17	0.20	0.16	0.33	0.23	0.20
<b>QYZ</b>	0.63	0.53	0.39	0.39	0.41	0.34	0.34	0.57	0.50	0.38
<b>DHS</b>	0.60	0.52	0.35	0.34	0.37	0.33	0.21	0.81	0.49	0.33
<b>YC</b>	0.57	0.31	0.19	0.18	0.21	0.18	0.14	0.34	0.28	0.18
<b>HB</b>	0.28	0.20	0.10	0.10	0.08	0.08	0.05	0.21	0.15	0.08
<b>NM</b>	0.25	0.17	0.13	0.11	0.10	0.11	0.09	0.17	0.14	0.12
<b>Average</b>	<b>0.45</b>	<b>0.33</b>	<b>0.23</b>	<b>0.22</b>	<b>0.22</b>	<b>0.21</b>	<b>0.17</b>	<b>0.41</b>	<b>0.30</b>	<b>0.22</b>
<b>DX</b>	0.43	0.11	0.06	0.06	0.03	0.04	0.03	0.12	0.08	0.04

527



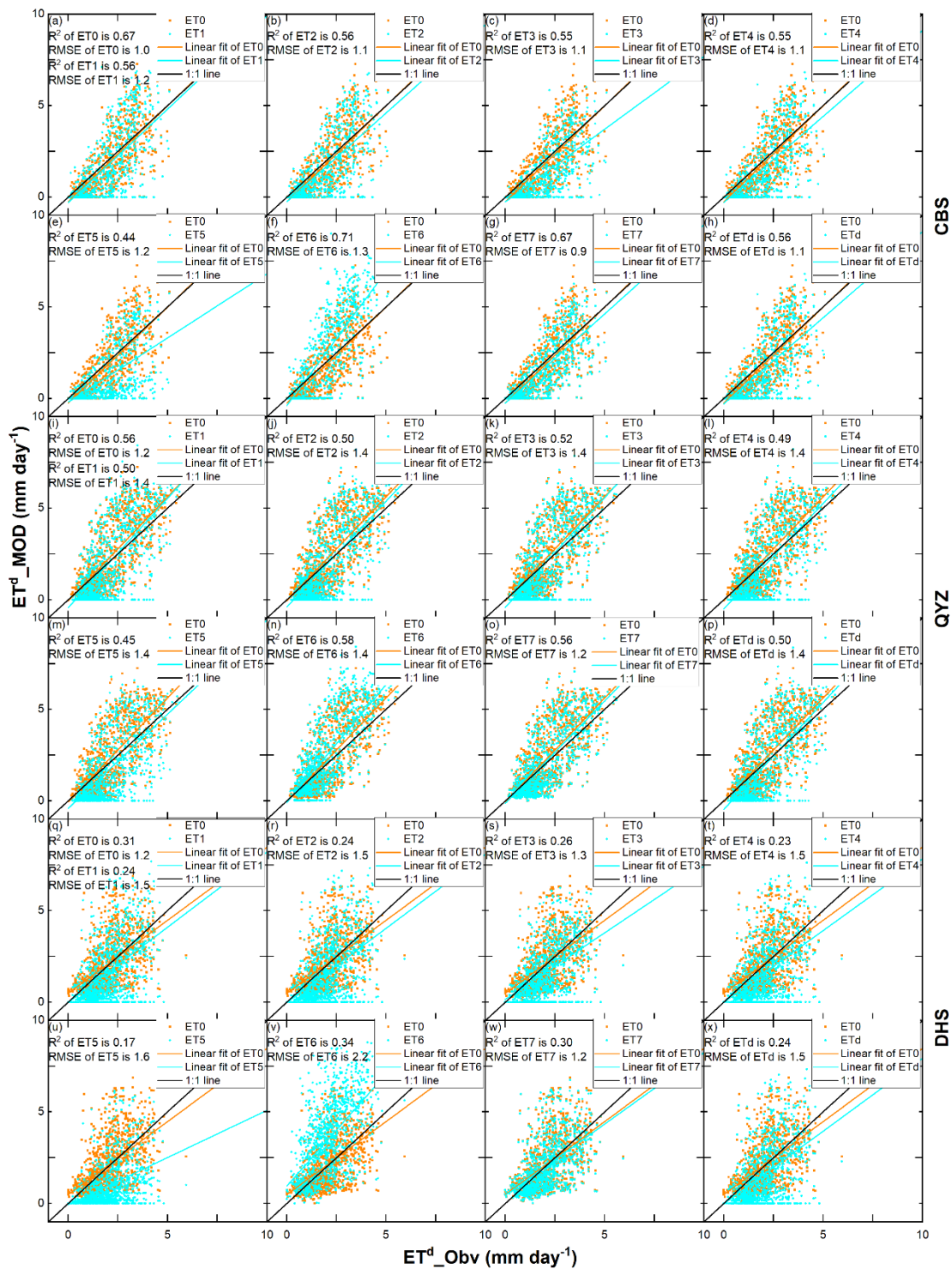
528

529 **Figure 7.** Comparison of multiyear averaged observed diurnal evaporation fraction,  
 530  $EF$  ( $EF\_Obv$ ) and estimated daily mean  $EF$  ( $EF0$ ,  $EF1$ ,  $EF2$ ,  $EF3$ ,  $EF4$ ,  $EF5$ ,  
 531  $EF6$ ,  $EF7$ , and  $EFd$ ) during 2003 to 2005 at Changbaishan (CBS), Qianyanzhou  
 532 (QYZ), Dinghushan (DHS), Yucheng (YC), Haibei (HB), Neimeng (NM) and

533 Dangxiong (DX)

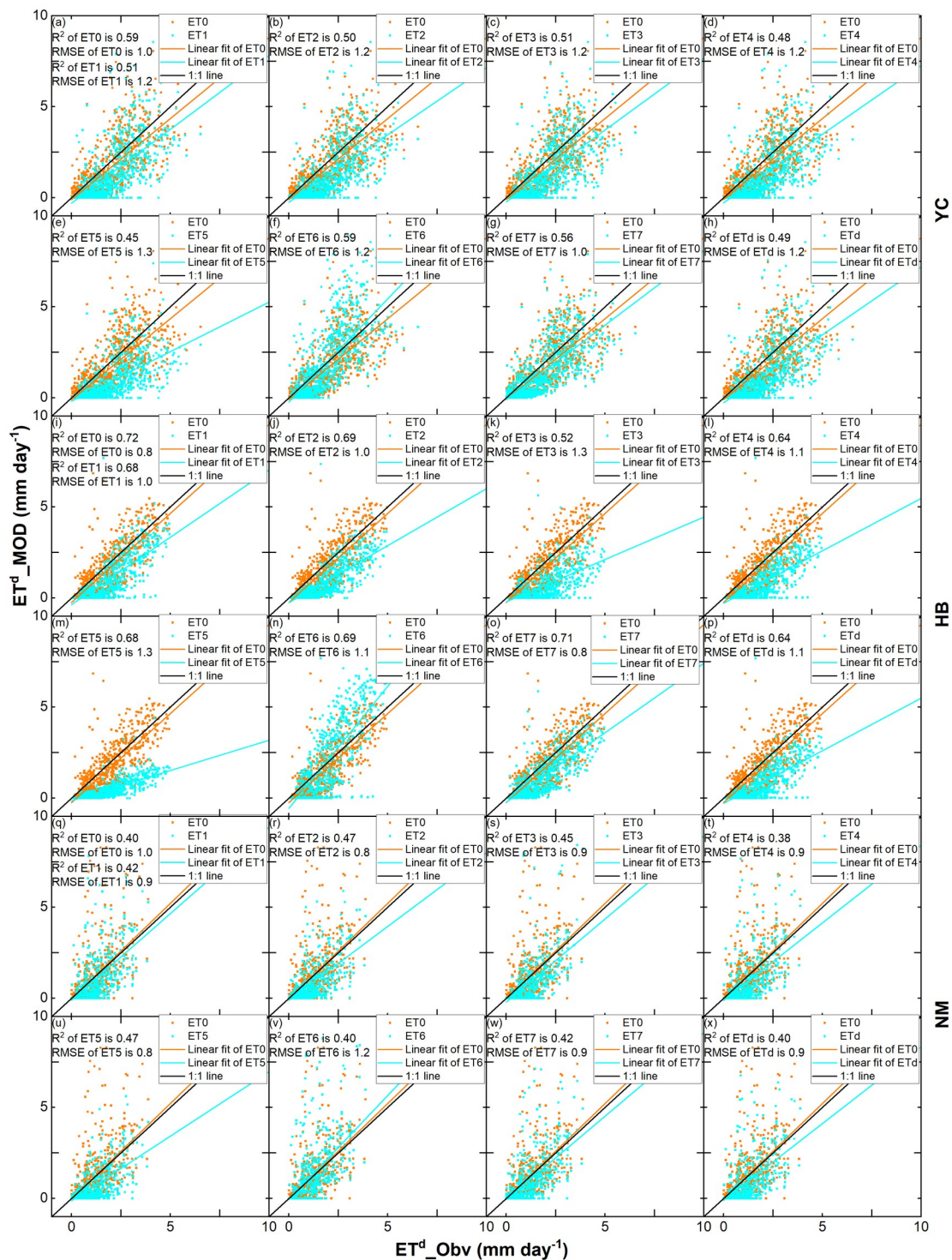
534 4.5 Evapotranspiration

535 The daily evapotranspiration calculated with the decoupling factor method (ET1  
 536 to ET7 and ETd in Table 1) is plotted against the flux tower measurements in Figure  
 537 8. The daily evaporation was obtained with Eq 15 by multiplying the evaporation  
 538 fraction  $EF^d$  (Table 3) with the daily available energy,  $Q$  (Appendix C). In each plot  
 539 in Figure 8, the daily evaporation calculated with the Nishida method (ET0 in Table 1)  
 540 is also plotted for comparison. The averaged daily measured and calculated  
 541 evaporation over the measurement period for each flux tower observation are shown  
 542 in Table 4. Similar to the evaporation fraction depicted in Table 3, the satellite-based  
 543 ET for Changbiashan, CBS (in the plot of (a)-(h) of Figure 8a), with the  $R^2$  around  
 544 0.55 and RMSE 1.1 mm day<sup>-1</sup> and Haibei, HB (in the plot of (i)-(p) of Figure 8b),  
 545 with  $R^2$  around 0.65 and RMSE 1.1 mm day<sup>-1</sup> agree most closely with the flux tower  
 546 measurements. The Dinghushan, DHS (in the plot of (q)-(x) of Figure 8a), with the  $R^2$   
 547 around 0.25 and RMSE 1.5 mm day<sup>-1</sup> and Dangxiong, DX (Figure 8c) with the  $R^2$   
 548 around 0.35 and RMSE 1.5 mm day<sup>-1</sup> deviate the farthest. Unlike the  $EF$  results in  
 549 Table 3, ET0 predicted most closely the flux tower measurements with the greatest  $R^2$ ,  
 550 lowest RMSE (Figure 8a-8c, and Table 4). The ET6 method that most closely  
 551 matched the observed  $EF^d$  value in Table 3 overpredicted the observed flux tower  
 552 measurements significantly with RMSE 1.1 to 2.2 mm day<sup>-1</sup> (Figure 8a-8c, and Table  
 553 4). Of the other methods that calculated the ET from the satellite data, ET1-ET4  
 554 underestimated the daily  $ET$  by nearly 50% and ET7 underestimated the daily  $ET$   
 555 by 30% (Table 4).



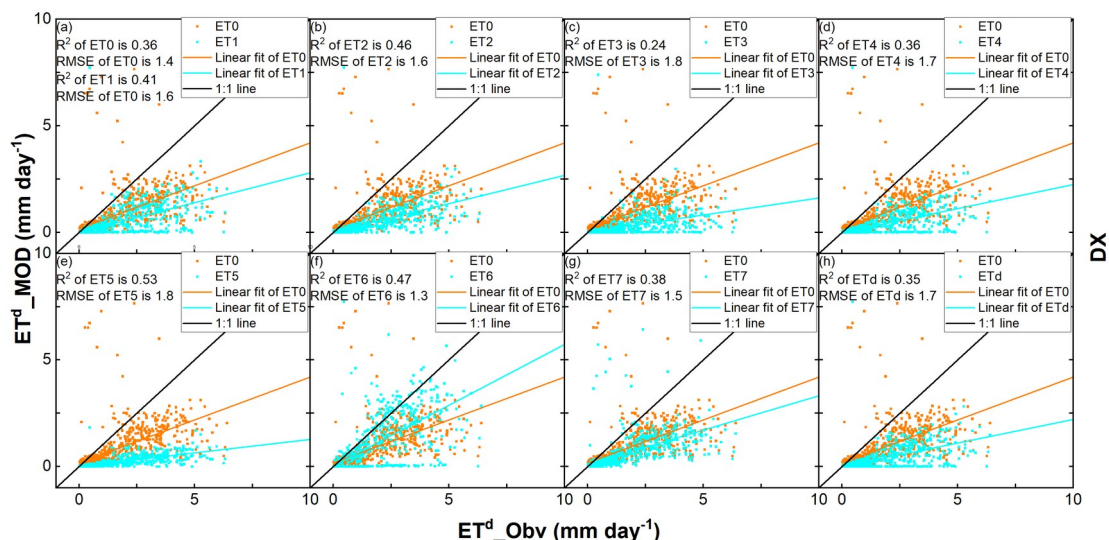
556

557 **Figure 8a.** Scatter plots of daily estimated *ET* data ET<sup>d</sup>\_MOD (ET0, ET1, ET2,  
 558 ET3, ET4, ET5 ET6, ET7 and ETd) against flux tower daily observed *ET* data  
 559 (ET<sup>d</sup>\_Obv) at entire period of 2003 to 2005 at Changbaishan (CBS), Qianyanzhou  
 560 (QYZ), Dinghushan (DHS) sites.



561

562 **Figure 8b.** Scatter plots of daily estimated *ET* data ETd\_MOD (ET0, ET1, ET2,  
 563 ET3, ET4, ET5 ET6, ET7 and ETd) against flux tower daily observed *ET* data  
 564 (ETd\_Obv) at entire period of 2003 to 2005 at Yucheng (YC), Haibei (HB) and 2004  
 565 to 2005 at Neimeng (NM) sites.



566

567 **Figure 8c.** Scatter plots of daily estimated *ET* data (ET0, ET1, ET2, ET3, ET4, ET5  
 568 ET6, ET7 and ETd) against flux tower daily observed *ET* data (ET\_Obv) at entire  
 569 period of 2004 to 2005 a) at Dangxiong (DX) site.

570 **Table 4.** The comparison of the flux tower observed daily mean *ET* (ET\_Obv) and  
 571 the satellite-based estimated *ET* with various methods (ET0-ET7 and ETd, ET6\_new  
 572 was calculated by the EF6 and the observed net radiation) during 2003 to 2005 at  
 573 Changbaishan (CBS), Qianyanzhou (QYZ), Dinghushan (DHS), Yucheng (YC),  
 574 Haibei (HB), Neimeng (NM) and Dangxiong (DX) sites.

Site	ET_Obv	ET0	ET1	ET2	ET3	ET4	ET5	ET6	ET7	ETd	ET6_new
	mm day <sup>-1</sup>										
<b>CBS</b>	1.44	1.25	1.16	1.14	0.87	1.05	0.80	1.71	1.14	1.05	1.65
<b>QYZ</b>	2.05	2.27	2.01	1.97	2.03	1.86	1.70	2.55	2.16	1.93	2.35
<b>DHS</b>	2.06	2.13	1.68	1.65	1.65	1.61	0.99	3.47	2.05	1.61	3.24
<b>YC</b>	1.64	1.36	1.03	0.97	1.06	0.96	0.71	1.63	1.24	0.95	1.46
<b>HB</b>	1.37	1.09	0.65	0.60	0.43	0.50	0.31	1.28	0.82	0.51	1.18
<b>NM</b>	0.96	0.92	0.74	0.62	0.64	0.64	0.49	1.03	0.77	0.65	0.61
<b>Average</b>	1.59	1.50	1.21	1.16	1.11	1.10	0.83	1.95	1.36	1.12	1.75
<b>DX</b>	1.50	0.80	0.43	0.43	0.27	0.34	0.20	0.93	0.60	0.34	0.53

575

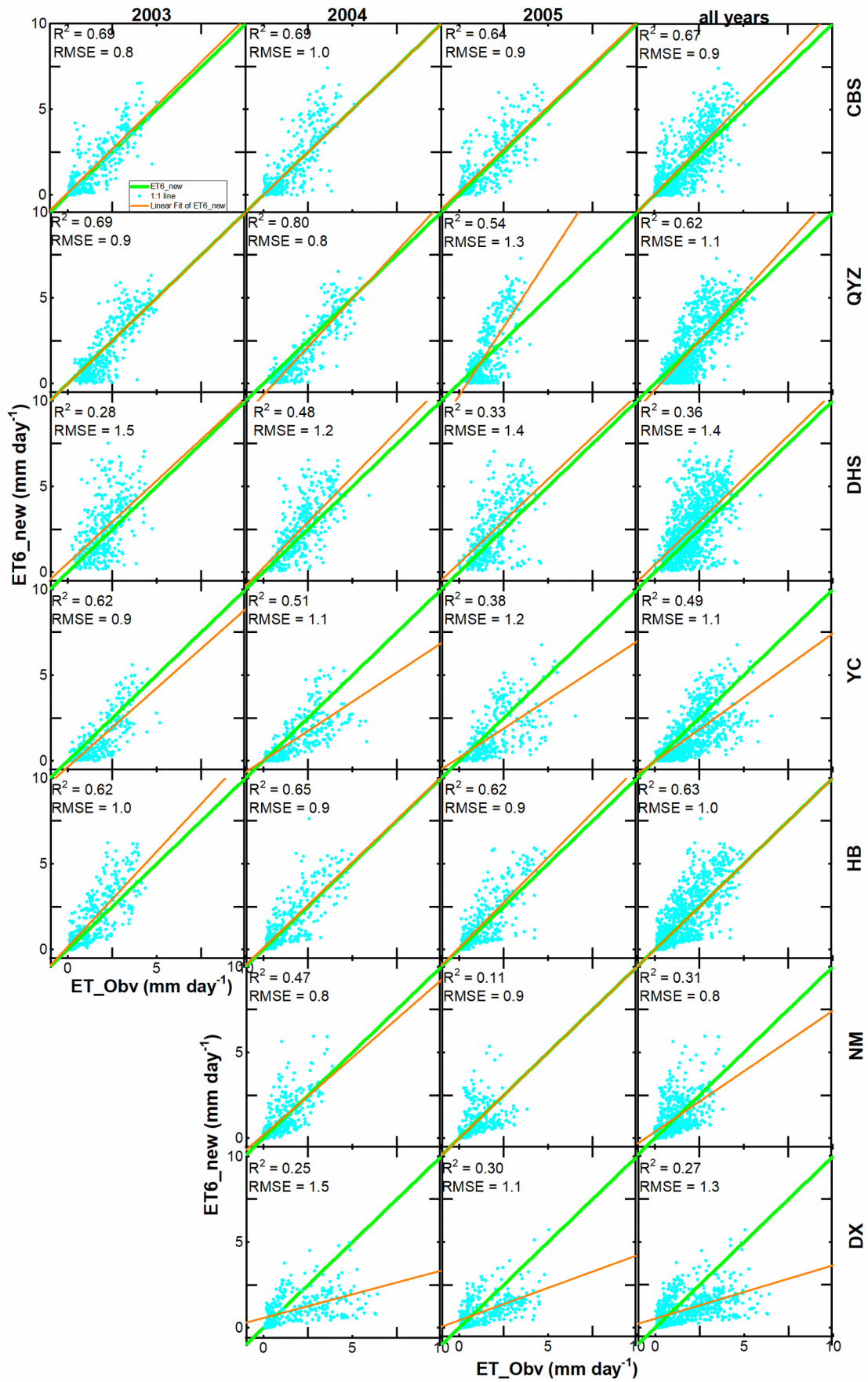
576 Considering the intermediate results in Fisections 4.1 to 4.4, the calculated *EF*  
 577 with the method of Nashida (2003), EF0, was on the average 25% less than the  
 578 observed flux tower *EF* (Figure 7 and Table 3). While the daily net radiation was 30%  
 579 greater than the flux tower measurement (Figur 4). Thus, the daily ET0 was predicted  
 580 more accurately than any other methods in Table 1. as it is the product of these two  
 581 variables (Eq. 15) fortuitously provided the correct answer. Conversely, the EF6

582 method predicted the *EF* most closely to the flux tower measurements but  
583 overpredicted the daily evaporation, because of the 30% overestimates of the daily net  
584 radiation (Figur 4).

585 To reduce the impact of the overestimated daily net radiaiton on the daily *ET*  
586 estimates and examine whether the ET6 method would accurately predict the  
587 evaporation, we used EF6 method and the observed flux tower net radiation to  
588 recalculate the ET. The results are shown in Figure 9. The calculated *ET* generally  
589 match the observations with  $R^2$  ranging from 0.27 to 0.67 and RMSE ranging from  
590 0.9 to 1.4 mm day<sup>-1</sup>. Compared to the ET0 method, the ET6 methad was generally  
591 more precise. For example, in the CBS site, the RMSE of ET6\_new and ET0 is 0.9  
592 mm day<sup>-1</sup> and 1.0 mm day<sup>-1</sup> respectively; in the QYZ site, the  $R^2$  is 0.62 (ET6\_new)  
593 and 0.56 (ET0), RMSE is 1.1 mm day<sup>-1</sup> (ET6\_new) and 1.2 mm day<sup>-1</sup> (ET0); in the  
594 YC site, the  $R^2$  is 0.49 (ET6\_new) and 0.31(ET0), RMSE is 1.1 mm day<sup>-1</sup> (ET6\_new),  
595 and 1.2 mm day<sup>-1</sup> (ET0); in the HB site, the  $R^2$  is 0.63 (ET6\_new) and 0.59 (ET0)  
596 respectively.

597

598



599 **Figure 9.** As Figure 3, but for daily estimated *ET* (ET6\_new) which was based on  
 600 the EF6 and observed net radiation against flux tower daily observed *ET* data

601 (ET\_Obv).

## 602 **5 Discussion and Conclusion**

603 This study converted the instantaneous satellite observation into daily evaporation  
604 fraction and actual evapotranspiration, for forests, grassland, cropland, and deserts for  
605 large-scale applications in China. Our approach was based on the decoupling  
606 parameter method introduced by Tang & Li (2017) for irrigated winter wheat and  
607 summer maize cropland in the North China Plain. The decoupling parameter method  
608 is based on the relative contribution of radiative and aerodynamic terms to the overall  
609 evapotranspiration. We introduced eight different ways to calculate the daily  
610 evaporation from instantaneous satellite observation by replacing none, one, or  
611 several of the daily calculated intermediate variables by their instantaneous values  
612 (EFd, EF1-EF7 in Table 1). In this way, we were able to check the validity of the  
613 proposed conversions of instantaneous to daily values.

614 The MODIS 0.05-degree grid cell data, rather than the 250m or 500 m, was used  
615 as input because our focus was on determining the *ET* for China. A better agreement  
616 could have been obtained between flux tower measurement and satellite-based  
617 calculations of evaporation and its intermediate calculated values by calibrating the  
618 vegetation coverage ( $f_{veg}$ ) in Eq. 2 using the same footprint MODIS data and flux  
619 tower surroundings. For example, for the DX site, the  $f_{veg}$  for the 0.05 grid cell is 0.13,  
620 and the  $f_{veg}$  for the flux tower footprint is 0.65. This resulted in a mismatch of satellite  
621 and flux tower evaporation. For this reason, the DX site was excluded from further  
622 consideration.

623 In evaluating the original Nishida method, we found that despite underestimating  
624 the evaporation fraction of the flux towers by 26% on average, the daily evaporation  
625 was more accurate than any of the eight methods based on the original Nishida  
626 method. The Nishida method assumed that the instantaneous evaporation was equal  
627 to the daily evaporation. By checking the intermediate values, we found that the daily  
628 net radiation was 30% too large. This too-large value with the 26% lower evaporation  
629 fraction made the daily *ET* estimates of the Nishada method came out well.

630 In calculating the daily net radiation, the diurnal albedo was assumed remained  
631 constant during the day. Studies (Cierniewski et al., 2015; Jääskeläinen & Manninen,  
632 2021; Wang et al., 2015; Zhang et al., 2020) have proven that the albedo has a distinct  
633 diurnal variation with the minimum values during the noon when the satellite  
634 overpass (Grant et al., 2000). Observations at the Wujiaqu site (Appendix I) in  
635 Northwest China confirmed the findings. Thus, assuming that the albedo was  
636 constant resulted in the overestimation of the daily net radiation. It affected the  
637 intermediate calculated values such as the daily decoupling resistance  $r^{i,d}$  in Eq. 11,  
638 where the daily net radiation is in the denominator. Other variables such as the daily  
639 decoupling parameter  $\Omega^{i,d}$ , depended on the value  $r^{i,d}$  (Eq. 12). Ultimately the 30%  
640 error in the daily net radiation caused about 50% and 30% or higher underestimates of  
641 daily  $EF$  and  $ET$  respectively for six of the eight methods of the decoupling parameter  
642 method in Table 1.

643 Once we dropped the decoupling parameter  $\Omega^{i,d}$  in determining the daily  $EF$  and  
644 used the correct daily net radiation, we found that the Tang & Li (2017) method as  
645 adapted by us and provided both reasonable daily  $EF$  and  $ET$  estimates with the  
646 relative error of 8% and 9% respectively. Thus using the decoupling parameter  
647 method should be tried in other locations as well for predicting the  $ET$  over large  
648 areas.

649

## 650 **Acknowledgments**

651 Funding for this research is provided by the The National Key Research and  
652 Development Program of China (NO.2017YFA0603703). The radiation dataset used  
653 in this study was developed by Ministry of Education Key Laboratory for Earth  
654 System Modeling, Department of Earth System Science, Tsinghua University and  
655 Center for Excellence in Tibetan Plateau Earth Sciences, Institute of Tibetan Plateau  
656 Research, Chinese Academy of Sciences. The flux tower data was provided by the  
657 Chinese FLUX Observation and Research Network. The authors declare no conflict of  
658 interest.

659 **Appendix A: Vegetation fraction ( $f_{veg}$ ) and Normalized Difference Vegetation**  
 660 **Index (NDVI)**

661

662 The vegetation fraction coverage ( $f_{veg}$ ) is calculated as (Figure 1)

$$663 \quad f_{veg} = \frac{NDVI - NDVI_{min}}{NDVI_{max} - NDVI_{min}} \quad (A1)$$

664 where the NDVI is the Normalized Difference Vegetation Index and can be calculated  
 665 as:

$$666 \quad NDVI = \frac{R_{nir} - R_i}{R_{nir} + R_i} \quad (A2)$$

667 where  $NDVI_{min}$  is the NDVI of the bare soil without plants and  $NDVI_{max}$  is the NDVI  
 668 of the full vegetation cover,  $R_{nir}$  is the near-infrared reflectance and  $R_i$  is the red  
 669 reflectance. The daily reflectance  $R_{nir}$  and  $R_i$  were measured by MODIS reflectance  
 670 data MOD09CMG (Figure 1). Based on Tang (2009), we have set  $NDVI_{min} = 0.22$  and  
 671  $NDVI_{max} = 0.83$ . Missing observation for the daily NDVI data was filled with the 16-  
 672 day averaged NDVI values in the MOD13Q1 data product (Fig. 1, Table 2).

673

674

675

676

677

678

679

680

681

682

683

684

685

686 **Appendix B: The calculation of the slope of the saturated vapor, and the vapor**  
 687 **pressure deficit of the air  $VPD$**

688

689 The slope of the saturated vapor ( $\Delta$ ),

$$690 \quad \Delta = 4098 \frac{\gamma}{T_a} \quad (B1)$$

691 where  $T_a$  is the air temperature ( $^{\circ}C$ ) that can be calculated by the VI-Ts method in  
 692 Appendix F with the NDVI and land surface data.  $VPD$  is the vapor pressure deficit of  
 693 the air (kPa)

$$694 \quad VPD = e^0(T_a) - e_a \quad (B2)$$

$$695 \quad e^0(T_a) = 0.6108 \exp \left( \frac{17.27 T_a}{T_a + 237.3} \right) \quad (B3)$$

$$696 \quad e_a = e^0(T_{dew}) \quad (B4)$$

$$697 \quad e^0(T_{dew}) = 0.6108 \exp \left[ \frac{17.27 T_{dew}}{T_{dew} + 237.3} \right] \quad (B5)$$

698 where the parenthesis indicates the independent variable,  $e^0(T_a)$  is the saturation vapor  
 699 pressure (kPa) at the air temperature  $T_a$  ( $^{\circ}C$ );  $e_a$  is the actual vapor pressure (kPa);

700  $e^0(T_{dew})$  is the saturation vapor pressure (kPa) at the dew point temperature  $T_{dew}$  ( $^{\circ}C$ ).

701  $T_{dew}$  is set to the minimum air temperature during the day ( $^{\circ}C$ ) for the forest, water  
 702 surface, and cropland. In arid areas like bare soil and non-irrigated grassland,  $T_{dew}$   
 703 maybe 2-3  $^{\circ}C$  lower than  $T_{min}$ . For this reason, 2  $^{\circ}C$  is subtracted from to the  $T_{min}$  in  
 704 arid and semiarid areas to obtain the  $T_{dew}$ . Although these simplifications might  
 705 introduce a bias in the final calculated  $ET$  value, our initial results showed that the  
 706 effect was small.

707

708 **Appendix C: Determining the net radiation ( $R_n$ ), available energy of bare soil ( $Q_{soil}$ ) and vegetation cover ( $Q_{veg}$ ).**

710

711 The net radiation was calculated by the land surface energy balance equation (Tang et  
712 al., 2009):

$$713 \quad R_n = (1 - albedo) R_d + \varepsilon \sigma (T_a - 20)^4 - \varepsilon \sigma T_s^4 \quad (C1)$$

714 where *albedo* is obtained from the MODIS 16-day albedo data (MCD43C3);  $R_d$  is the  
715 3-hourly incoming shortwave radiation from the China Meteorological Forcing  
716 Datasets (CMFD) ( $\text{W m}^{-2}$ ) with a resolution of 0.1 degrees;  $\varepsilon$  is the emissivity from  
717 the MODIS daily surface temperature/emissivity data (MOD11C1);  $\sigma$  is the Stefan-  
718 Boltzmann constant  $5.6704 \times 10^{-8} \text{ W m}^{-2} \text{ K}^{-4}$ ;  $T_a$  is the air temperature (K);  $T_s$  is the  
719 surface temperature (K);  $\varepsilon \sigma (T_a - 20)^4$  is the incoming long-wave radiation ( $\text{W m}^{-2}$ ),

720  $\varepsilon \sigma T_s^4$  is the upward long-wave radiation ( $\text{W m}^{-2}$ ).

721 We follow Nishida (2003) to estimate the net radiation of vegetation  $R_{veg}$  ( $\text{W m}^{-2}$ ) by  
722 assuming  $T_s = T_a$

$$723 \quad R_{veg} = (1 - albedo) R_d + \varepsilon \sigma (T_a - 20)^4 - \varepsilon \sigma T_a^4 \quad (C2)$$

724 And we estimate the net radiation of bare soil  $R_{soil}$  ( $\text{W m}^{-2}$ ) following Nishida (2003),

725 assuming  $\varepsilon \sigma T_s^4 = \varepsilon \sigma T_a^4 + 4 \varepsilon \sigma T_a^3 (T_s - T_a)$

$$726 \quad R_{soil} = (1 - albedo) R_d + \varepsilon \sigma (T_a - 20)^4 - \varepsilon \sigma T_a^4 - c 4 \varepsilon \sigma T_a^3 (T_s - T_a) \quad (C3)$$

727 The available energy for the bare soil  $Q_{soil}$  ( $\text{W m}^{-2}$ ), and for fully vegetated surfaces,  
728  $Q_{veg}$  ( $\text{W m}^{-2}$ ) and the maximum available energy for evaporation of bare soil,  $Q_{soil}$  ( $\text{W}$   
729  $\text{m}^{-2}$ ) can be determined according to Nishida, (2003) as:

$$730 \quad Q_{soil} \approx (1 - C_G) (R_{n0} - 4 \varepsilon \sigma T_a^3 (T_{soil} - T_a)) \quad (C4)$$

$$731 \quad Q_{veg} = R_{n0} \quad (C5)$$

122

123

732 where the  $C_G$  is an empirical coefficient ranging from 0.3 (wet soil) to 0.5 (dry soil)  
733 (Idso et al., 1975);  $R_{n0}$  is the net radiation assuming  $T_{soil}$  equals  $T_a$  ( $\text{W m}^{-2}$ );  $T_{soil}$  is the  
734 surface temperature of bare soil (K) calculated with the VI-Ts diagram (Appendix F);

735 **Appendix D: determining the aerodynamic and surface resistance of bare soil**  
 736 **from satellite data**

737

738 The aerodynamic resistance of the bare soil,  $r_{a\ soil}$  ( $\text{m s}^{-1}$ ), was calculated by Nishida,  
 739 (2003), assuming that the maximum surface temperature of bare soil  $T_{soil\ max}$  (K)  
 740 occurs when the sum of latent heat flux and the sensible heat flux of the bare soil,  
 741 namely, the available energy of bare soil  $Q_{soil}$  ( $\text{W m}^{-2}$ ) is used as sensible heat flux and  
 742 the latent heat flux is zero:

$$743 \quad r_{a\ soil} = \frac{\rho C_p (T_{soil\ max} - T_a)}{Q_{soil}} \quad (\text{D1})$$

744  $r_{a\ soil}$  is the aerodynamic resistance of the bare soil, ( $\text{s m}^{-1}$ ),  $\rho$  is the air density,  $\text{kg m}^{-3}$ ;  
 745  $C_p$  is the specific heat of the air, ( $\text{J kg}^{-1} \text{K}^{-1}$ );  $T_{soil\ max}$  is the maximum surface  
 746 temperature of bare soil (K), calculated by the VI-Ts method in Appendix F,  $T_a$  is the  
 747 air temperature (K),  $Q_{soil}$  is the available energy of bare soil ( $\text{W m}^{-2}$ ).

748 For the calculation of canopy surface resistance of bare soil  $r_{c\ soil}$  ( $\text{s m}^{-1}$ ), we  
 749 follow the studies of Griend and Owe (1994), and Mu (2007):

$$750 \quad r_{c\ soil} = r_{tot} - r_{a\ soil} \quad (\text{D2})$$

$$751 \quad r_{tot} = \frac{1.0}{\left(\frac{T_a}{293.15}\right)^{1.75} \frac{101300}{P}} * 107.0 \quad (\text{D3})$$

752 where  $r_{tot}$  is the total aerodynamic resistance ( $\text{s m}^{-1}$ );  $r_{a\ soil}$  is the aerodynamic  
 753 resistance over the bare soil ( $\text{s m}^{-1}$ );  $P$  is the atmospheric pressure (Pa), which was set  
 754 to 101300 Pa.

755

756 **Appendix E: Determining the surface resistance and aerodynamic of a vegetation**  
 757 **canopy from satellite data**

758

759 Jarvis (1976) found that the inverse of surface resistance of the canopy  $\frac{1}{r_{cveg}}$  is equal

760 to:

$$761 \quad \frac{1}{r_{cveg}} = \frac{f_1(T_a)f_2(PAR)f_3(VPD)f_4(\phi)f_5(CO_2)}{r_{cMIN}} + \frac{1}{r_{cuticle}} \quad (E1)$$

762 where  $r_{cMIN}$  is the minimum resistance ( $s\ m^{-1}$ );  $r_{cMIN} = 33$  ( $s\ m^{-1}$ ) for cropland and  
 763  $r_{cMIN} = 50$  ( $s\ m^{-1}$ ) for all other vegetation (Tang, 2009);  $r_{cuticle}$  is the canopy resistance  
 764 related to diffusion through the cuticle layer of leaves ( $s\ m^{-1}$ ). The value used in the  
 765 Biome-BGC model is  $r_{cuticle} = 100,000$  ( $s\ m^{-1}$ , White et al., 2000), which is used by us.

766 The functions of air temperature  $T_a$ ,  $f_1(T_a)$  and photosynthetic active radiation  $PAR$ ,

767  $f_2(PAR)$  can be written as (Jarvis, 1975):

$$768 \quad f_1(T_a) = \left( \frac{T_a - T_n}{T_o - T_n} \right) \left( \frac{T_x - T_a}{T_x - T_o} \right)^{\frac{T_x - T_o}{T_o - T_n}} \quad (E2)$$

769 where  $T_n$ ,  $T_o$  and  $T_x$  are the minimum, optimal and maximum temperature for  
 770 stomatal activity. According to Tang (2009),  $T_n = 275.85$  K,  $T_o = 304.25$  K and  $T_x =$   
 771  $318.45$  K. The function  $f_2(PAR)$  is expressed as:

$$772 \quad f_2(PAR) = \frac{PAR}{PAR + A} \quad (E3)$$

773 where  $PAR$  is photosynthetic active radiation per unit area and time ( $\mu\ mol\ m^{-2}\ s^{-1}$ )  
 774 calculated by incoming solar radiation multiplied by 2.05 (Campbell and Norman,  
 775 2000);  $A$  is a parameter related to photon absorption efficiency at low light intensity,  
 776 which was set to  $152\ \mu\ mol\ m^{-2}\ s^{-1}$  (Tang, 2009); Nishida (2003) found that in Eq. E1  
 777 the following functions can be omitted without great loss of accuracy: the functions  
 778 depending on vapor pressure deficit,  $f_3(VPD)$ , leaf water potential  $f_4(\phi)$  and carbon

779 dioxide vapor pressure,  $f_5(CO_2)$ .

780 Instantaneous and daily aerodynamic resistance of the canopy  $r_{a\,veg}$  ( $s\ m^{-1}$ ) is  
 781 calculated by the empirical formulae of Kondo (2000) for forest cover, grassland, and  
 782 cropland:

$$783 \quad \frac{1}{r_{a\,veg(forest)}} = 0.008 U_{50m} \quad (E4)$$

784 where  $U_{50m}$  is the wind speed at 50 m height above the canopy ( $m\ s^{-1}$ ). The  
 785 aerodynamic resistance grassland and cropland is Kondo (2000)

$$786 \quad \frac{1}{r_{a\,veg(grassland \wedge cropland)}} = 0.003 U_{1m} \quad (E5)$$

787 where  $U_{1m}$  is the wind speed 1m above the canopy ( $m\ s^{-1}$ ). The wind speed as a  
 788 function of the height  $z$ ,  $U(z)$  can be calculated by the logarithm profile of wind. As  
 789 the  $r_{a\,veg}$  has two variety calculation equations (E4 and E5) in the forest canopy (E4),  
 790 grassland and cropland (E5), thus, we used the land cover classes from the yearly  
 791 International Geosphere-Biosphere Programme (IGBP) (MCD12C1) to identify the  
 792 land cover and choice the different equation of  $r_{a\,veg}$ .  $U_{50m}$  and  $U_{1m}$  were calculated by  
 793 the logarithm profile of wind:

$$794 \quad U(z) = U_{shear} \ln \left[ \frac{(z-d)}{z_0} \right] / k \quad (E6)$$

795 where  $U_{shear}$  is the shear velocity ( $m\ s^{-1}$ );  $z$  is the height (m);  $d$  is the surface  
 796 displacement (m);  $z_0$  is the roughness length, we followed Kondo (2000), set as 0.005  
 797 m for bare soil and 0.01 m for grassland;  $k$  is the von Karman's constant and set as 0.4  
 798 following Nishida (2003). The shear velocity  $U_{shear}$  was calculated as:

$$799 \quad U_{shear} = U_{1msoil} \frac{0.4}{\ln \left( \frac{1}{0.005} \right)}$$

800 ( $m\ s^{-1}$ ), it was calculated as:

$$801 \quad U_{1msoil} = 1/0.0015 r_{a\,soil} \quad (E7)$$

802 The instantaneous air temperature can be calculated by the Vegetation Index-  
 803 surface Temperature (VI-T<sub>s</sub>) diagram (Nishida et al., 2003) using MODIS  
 804 instantaneous surface temperature/emissivity data (MOD11C1) and daily calculated

805 NDVI as inputs (Appendix F).

806

807

808

809

810

811

812

813 **Appendix F Calculating instantaneous air temperature based on the VI-Ts**

814 **diagram**

815

816 The calculation progress of instantaneous air temperature is shown in Appendix

817 (a), the scatter plot of vegetation index (VI) versus land surface temperature (Ts) is

818 drawn like Appendix (b). The slope of the warm edge can be calculated according to

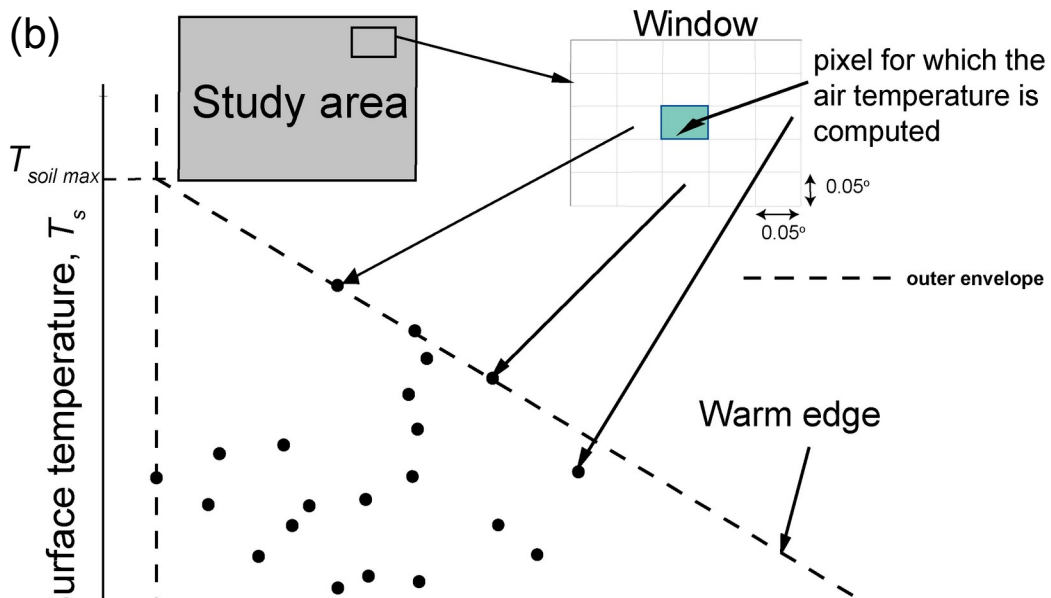
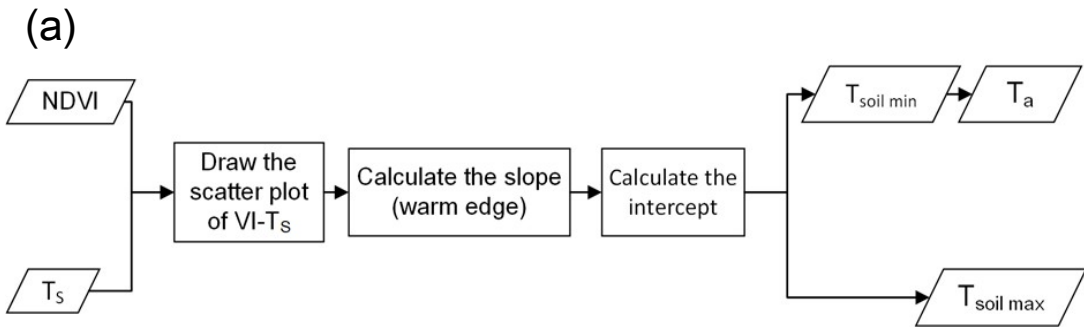
819 the slope and the maximum and minimum NDVI, by which, we can get the  $T_{soil\ min}$  and

820  $T_{soil\ max}$  as the intercept of the slope. At last, we assumed that the  $T_{soil\ min}$  equals to the

821 instantaneous air temperature  $T_a^i$ .

822

823





139

824 **Figure F1:** Calculating instantaneous air temperature based on the VI-Ts diagram. (a)  
 825 is the calculation progress of the instantaneous air temperature and (b) is the scatter  
 826 plot of the vegetation index and the surface temperature.

827

828

829

830

831

832

833

834

835

836

837 **Appendix G. The flowchart daily air temperature of calculation**

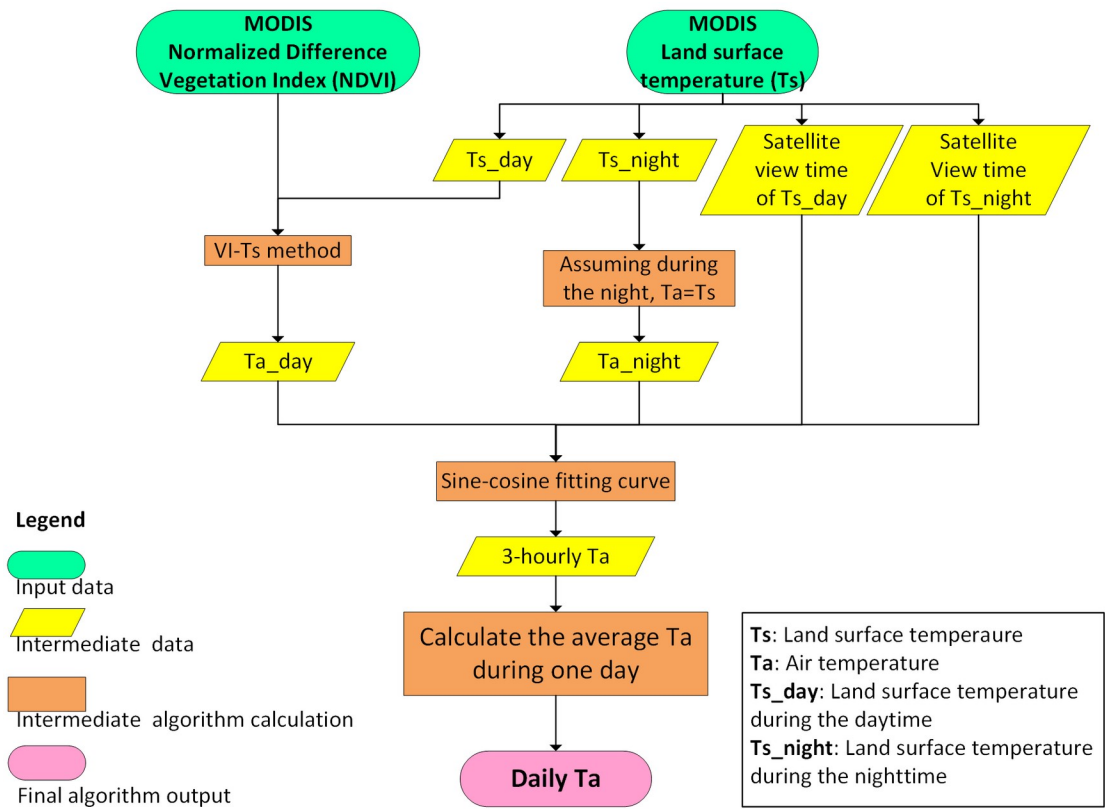
838 The daily mean air temperature  $T_a^d$  (K) was calculated as the average of 8 3-  
 839 hourly air temperature estimates (Figure G1). These 3-hourly air temperature

840 estimates were interpolated by the instantaneous air temperature  $T_a^i$  and the

841 instantaneous night air temperature (which was assumed to be equal to the MODIS

842 land surface temperature during the night) based on a sine-cosine fitting curve.

843



844

845 **Figure G1:** The flowchart daily air temperature of calculation.

846

847

848

849

850

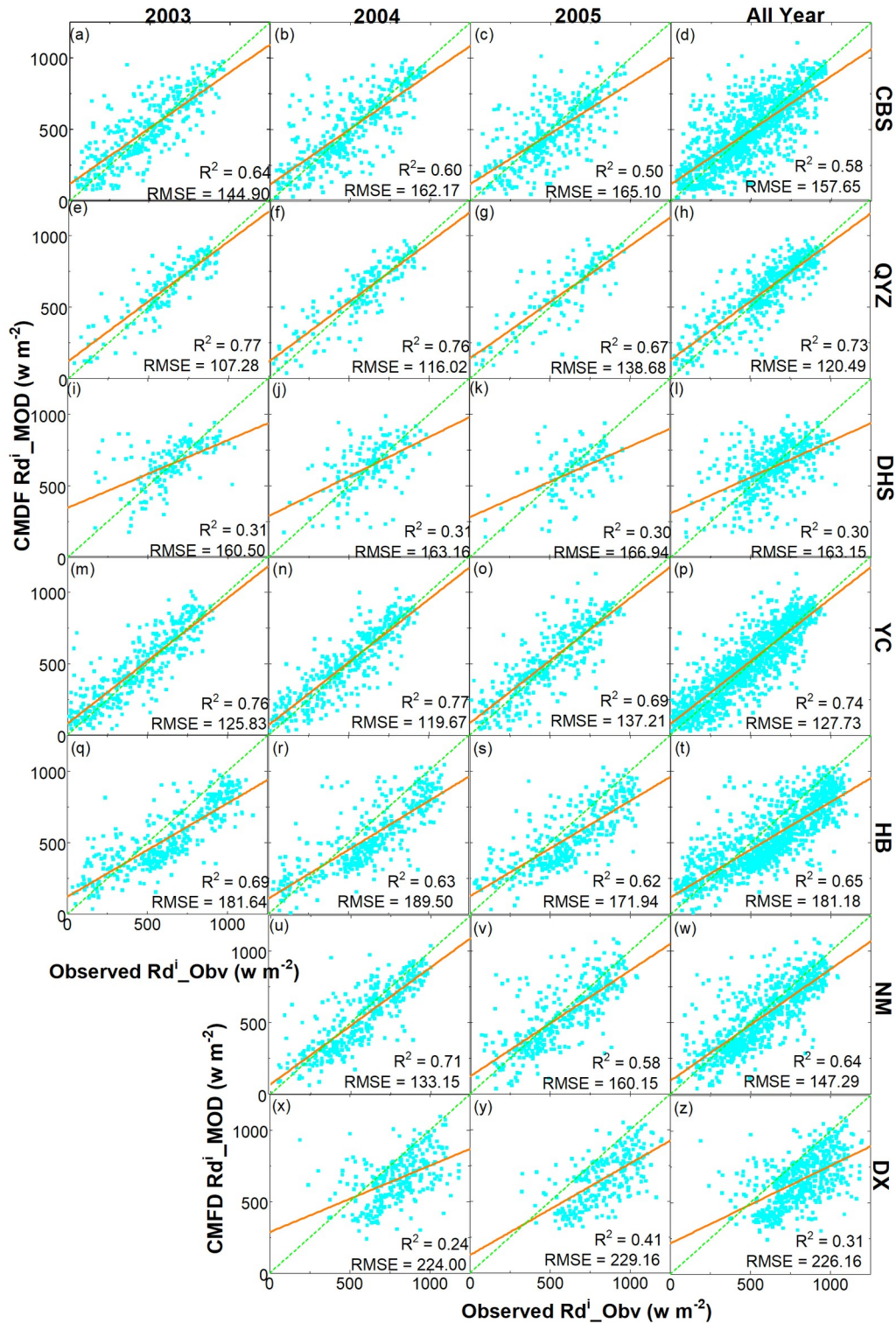
851

852

853

854

855 **Appendix H: shortwave radiation validation**

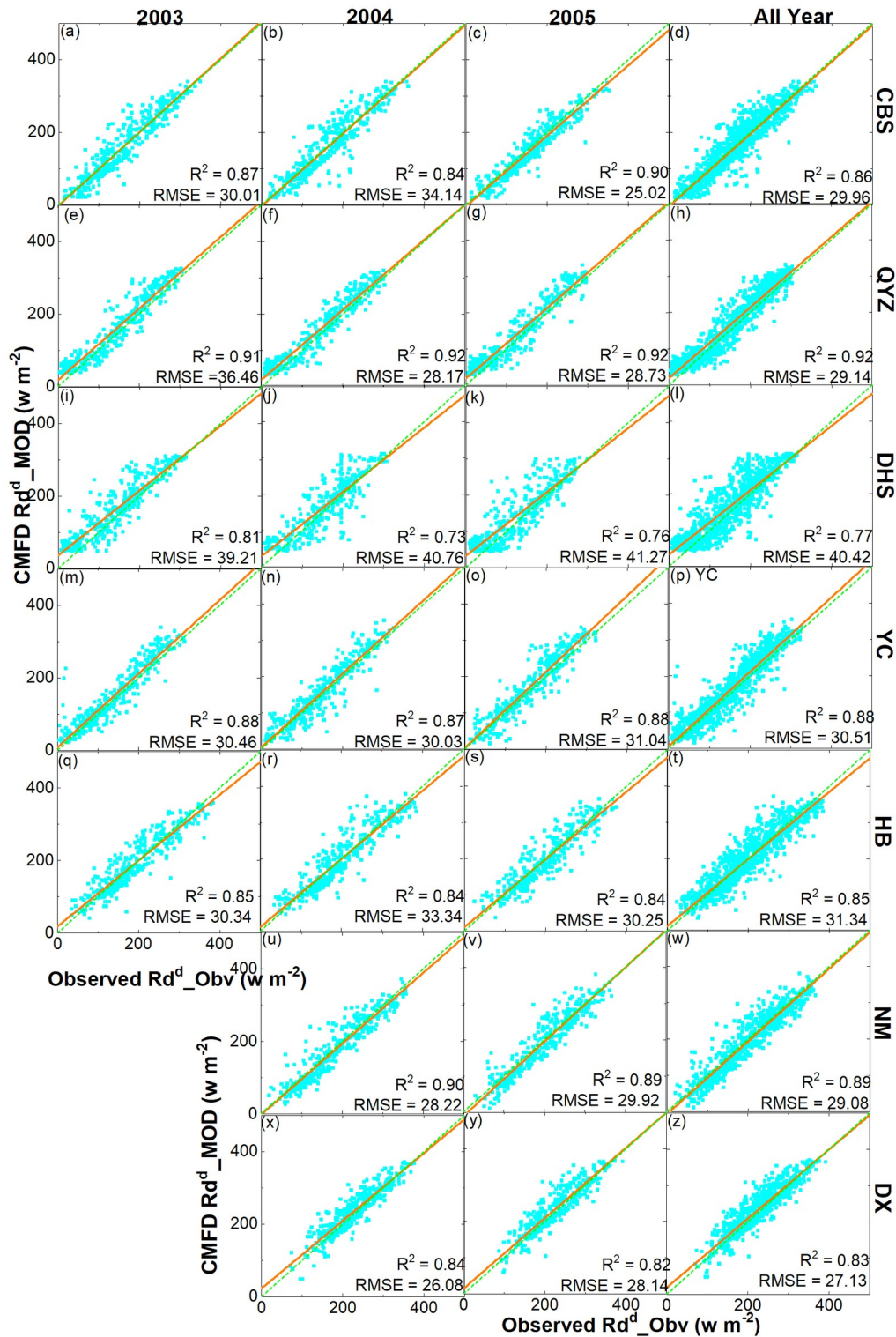


856

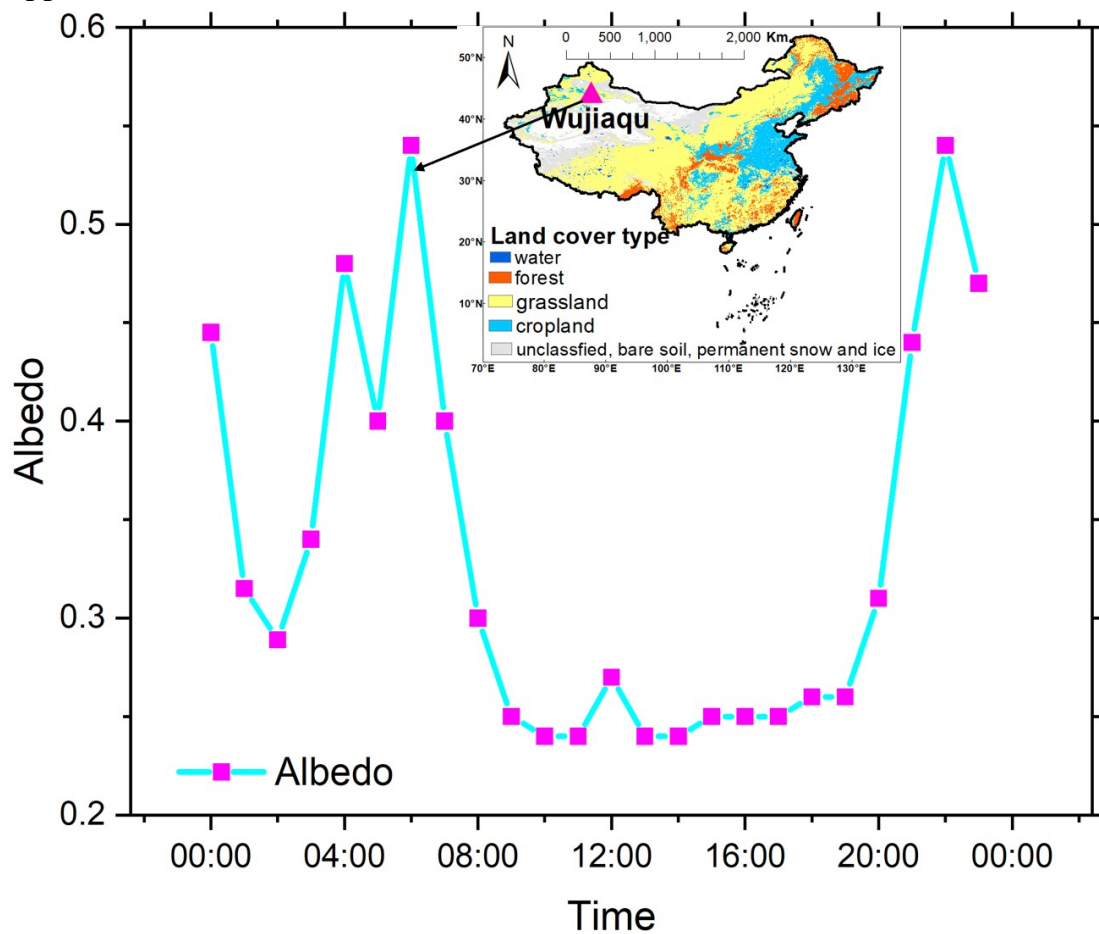
857 **Figure H1.** Instantaneous satellite-based shortwave radiation from the China  
 858 Meteorolgy Forcing Dataset (CMFD), Rd<sup>i</sup>\_MOD against flux tower observed  
 859 instantaneous download, shortwave radiation Rd<sup>i</sup>\_Obv. From  
 860 [https://www.spiedigitallibrary.org/journals/Journal-of-Applied-Remote-Sensing/](https://www.spiedigitallibrary.org/journals/Journal-of-Applied-Remote-Sensing/volume-11/issue-02/026019/Evaluation-of-satellite-based-evapotranspiration-estimates-in-China/10.1117/1.JRS.11.026019.full)  
 861 volume-11/issue-02/026019/Evaluation-of-satellite-based-evapotranspiration-  
 862 estimates-in-China/10.1117/1.JRS.11.026019.full. Reprinted with permission.  
 863

146

147



864  
 865 **Figure H2** Daily mean download shortwave radiation from the China Meteorology  
 866 Forcing Dataset (CMFD)  $Rd^d\_MOD$  against flux tower observed daily mean  
 867 download shortwave radiation ( $Rd^d\_Obv$ ). From  
 868 [https://www.spiedigitallibrary.org/journals/Journal-of-Applied-Remote-Sensing/](https://www.spiedigitallibrary.org/journals/Journal-of-Applied-Remote-Sensing/volume-11/issue-02/026019/Evaluation-of-satellite-based-evapotranspiration-estimates-in-China/10.1117/1.JRS.11.026019.full)  
 869 volume-11/issue-02/026019/Evaluation-of-satellite-based-evapotranspiration-  
 870 estimates-in-China/10.1117/1.JRS.11.026019.full. Reprinted with permission.

871 **Appendix I: The diurnal variation of albedo**

872

873 **Figure I:** The multimonth averaged observed diurnal albedo during Feb.2 to Dec.27  
 874 2020 at Wujiaqu flux tower site.

875

876

877

878 **References**

- 879 Ait Hssaine, B., Merlin, O., Ezzahar, J., Ojha, N., Er-Raki, S., & Khabba, S. (2020). An  
 880 evapotranspiration model self-calibrated from remotely sensed surface soil moisture, land  
 881 surface temperature and vegetation cover fraction: application to disaggregated SMOS  
 882 and MODIS data. *Hydrology and Earth System Sciences*, 24(4), 1781–1803.  
 883 <https://doi.org/10.5194/hess-24-1781-2020>
- 884 Alfieri, J. G., Anderson, M. C., Kustas, W. P., & Cammalleri, C. (2017). Effect of the revisit  
 885 interval and temporal upscaling methods on the accuracy of remotely sensed  
 886 evapotranspiration estimates. *Hydrology and Earth System Sciences*, 21(1), 83–98. <https://doi.org/10.5194/hess-21-83-2017>
- 888 Allen Richard G., Tasumi Masahiro, & Trezza Ricardo. (2007). Satellite-Based Energy Balance  
 889 for Mapping Evapotranspiration with Internalized Calibration (METRIC)—Model.  
 890 *Journal of Irrigation and Drainage Engineering*, 133(4), 380–394.

152

153

- 891 [https://doi.org/10.1061/\(ASCE\)0733-9437\(2007\)133:4\(380\)](https://doi.org/10.1061/(ASCE)0733-9437(2007)133:4(380))
- 892 Bastiaanssen, W. G. M., Menenti, M., Feddes, R. A., & Holtslag, A. A. M. (1998). A remote  
893 sensing surface energy balance algorithm for land (SEBAL). 1. Formulation. *Journal of*  
894 *Hydrology*, 212–213, 198–212. [https://doi.org/10.1016/S0022-1694\(98\)00253-4](https://doi.org/10.1016/S0022-1694(98)00253-4)
- 895 Bastiaanssen, W. G. M., Pelgrum, H., Wang, J., Ma, Y., Moreno, J. F., Roerink, G. J., & van der  
896 Wal, T. (1998). A remote sensing surface energy balance algorithm for land (SEBAL).:  
897 Part 2: Validation. *Journal of Hydrology*, 212–213, 213–229.  
898 [https://doi.org/10.1016/S0022-1694\(98\)00254-6](https://doi.org/10.1016/S0022-1694(98)00254-6)
- 899 Brutsaert, W., & Sugita, M. (1992). Application of self-preservation in the diurnal evolution of the  
900 surface energy budget to determine daily evaporation. *Journal of Geophysical Research:*  
901 *Atmospheres*, 97(D17), 18377–18382. <https://doi.org/10.1029/92JD00255>
- 902 Brutsaert, W., Cheng, L., & Zhang, L. (2019). Spatial Distribution of Global Landscape  
903 Evaporation in the Early Twenty First Century by Means of a Generalized  
904 Complementary Approach. *Journal of Hydrometeorology*. [https://doi.org/10.1175/JHM-](https://doi.org/10.1175/JHM-D-19-0208.1)  
905 [D-19-0208.1](https://doi.org/10.1175/JHM-D-19-0208.1)
- 906 Cammalleri, C., Anderson, M. C., & Kustas, W. P. (2014). Upscaling of evapotranspiration fluxes  
907 from instantaneous to daytime scales for thermal remote sensing applications. *Hydrology*  
908 *and Earth System Sciences*, 118(5), 1885–1894. <https://doi.org/10.5194/hess-18-1885-2014>
- 909 Chávez, J. L., Neale, C. M. U., Prueger, J. H., & Kustas, W. P. (2008). Daily evapotranspiration  
910 estimates from extrapolating instantaneous airborne remote sensing ET values. *Irrigation*  
911 *Science*, 27(1), 67–81. <https://doi.org/10.1007/s00271-008-0122-3>
- 912 Chen, J. M., & Liu, J. (2020). Evolution of evapotranspiration models using thermal and  
913 shortwave remote sensing data. *Remote Sensing of Environment*, 237, 111594.  
914 <https://doi.org/10.1016/j.rse.2019.111594>
- 915 Cierniewski, J., Karnieli, A., Kaźmierowski, C., Królewicz, S., Piekarczyk, J., Lewińska, K., et al.  
916 (2015). Effects of Soil Surface Irregularities on the Diurnal Variation of Soil Broadband  
917 Blue-Sky Albedo. *IEEE Journal of Selected Topics in Applied Earth Observations and*  
918 *Remote Sensing*, 8(2), 493–502. <https://doi.org/10.1109/JSTARS.2014.2330691>
- 919 Crago, R., & Brutsaert, W. (1996). Daytime evaporation and the self-preservation of the  
920 evaporative fraction and the Bowen ratio. *Journal of Hydrology*, 178(1), 241–255. [https://doi.org/10.1016/0022-1694\(95\)02803-X](https://doi.org/10.1016/0022-1694(95)02803-X)
- 922 Delogu, E., Boulet, G., Oliso, A., Coudert, B., Chirouze, J., Ceschia, E., et al. (2012).  
923 Reconstruction of temporal variations of evapotranspiration using instantaneous estimates  
924 at the time of satellite overpass. *Hydrology and Earth System Sciences*, 16(8), 2995–3010.  
925 <https://doi.org/10.5194/hess-16-2995-2012>
- 926 Dile, Y. T., Ayana, E. K., Worqlul, A. W., Xie, H., Srinivasan, R., Lefore, N., et al. (2020).  
927 Evaluating satellite-based evapotranspiration estimates for hydrological applications in  
928 data-scarce regions: A case in Ethiopia. *Science of The Total Environment*, 743, 140702.  
929 <https://doi.org/10.1016/j.scitotenv.2020.140702>
- 930 Faisol, A., Indarto, Novita, E., & Budiyo. (2020). An evaluation of MODIS global  
931 evapotranspiration product (MOD16A2) as terrestrial evapotranspiration in East Java -  
932 Indonesia. *IOP Conference Series: Earth and Environmental Science*, 485, 012002.  
933 <https://doi.org/10.1088/1755-1315/485/1/012002>
- 934 Gentine, P., Entekhabi, D., Chehbouni, A., Boulet, G., & Duchemin, B. (2007). Analysis of  
155  
156

- 935 evaporative fraction diurnal behaviour. *Agricultural and Forest Meteorology*, 143(1), 13–  
 936 29. <https://doi.org/10.1016/j.agrformet.2006.11.002>
- 937 Grant, I. F., Prata, A. J., & Cechet, R. P. (2000). The Impact of the Diurnal Variation of Albedo on  
 938 the Remote Sensing of the Daily Mean Albedo of Grassland. *Journal of Applied  
 939 Meteorology and Climatology*, 39(2), 231–244. [https://doi.org/10.1175/1520-0450\(2000\)039<0231:TIOTDV>2.0.CO;2](https://doi.org/10.1175/1520-0450(2000)039<0231:TIOTDV>2.0.CO;2)
- 941 He, J., Yang, K., Tang, W., Lu, H., Qin, J., Chen, Y., & Li, X. (2020). The first high-resolution  
 942 meteorological forcing dataset for land process studies over China. *Scientific Data*, 7(1),  
 943 25. <https://doi.org/10.1038/s41597-020-0369-y>
- 944 Hou, M., Tian, F., Zhang, L., Li, S., Du, T., Huang, M., & Yuan, Y. (2019). Estimating Crop  
 945 Transpiration of Soybean under Different Irrigation Treatments Using Thermal Infrared  
 946 Remote Sensing Imagery. *Agronomy*, 9(1), 8. <https://doi.org/10.3390/agronomy9010008>
- 947 Hu, X., Shi, L., Lin, L., & Zha, Y. (2019). Nonlinear boundaries of land surface temperature–  
 948 vegetation index space to estimate water deficit index and evaporation fraction.  
 949 *Agricultural and Forest Meteorology*, 279, 107736.  
 950 <https://doi.org/10.1016/j.agrformet.2019.107736>
- 951 Huang, L., Li, Z., Tang, Q., Zhang, X., Liu, X., & Cui, H. (2017). Evaluation of satellite-based  
 952 evapotranspiration estimates in China. *Journal of Applied Remote Sensing*, 11(2), 026019.  
 953 <https://doi.org/10.1117/1.JRS.11.026019>
- 954 Jääskeläinen, E., & Manninen, T. (2021). The effect of snow at forest floor on boreal forest albedo  
 955 diurnal and seasonal variation during the melting season. *Cold Regions Science and  
 956 Technology*, 185, 103249. <https://doi.org/10.1016/j.coldregions.2021.103249>
- 957 Jackson, R. D., Hatfield, J. L., Reginato, R. J., Idso, S. B., & Pinter, P. J. (1983). Estimation of  
 958 daily evapotranspiration from one time-of-day measurements. *Agricultural Water  
 959 Management*, 7(1), 351–362. [https://doi.org/10.1016/0378-3774\(83\)90095-1](https://doi.org/10.1016/0378-3774(83)90095-1)
- 960 Jung, M., Koirala, S., Weber, U., Ichii, K., Gans, F., Camps-Valls, G., et al. (2019). The  
 961 FLUXCOM ensemble of global land-atmosphere energy fluxes. *Scientific Data*, 6(1), 1–  
 962 14. <https://doi.org/10.1038/s41597-019-0076-8>
- 963 Knipper, K. R., Kustas, W. P., Anderson, M. C., Nieto, H., Alfieri, J. G., Prueger, J. H., et al.  
 964 (2020). Using high-spatiotemporal thermal satellite ET retrievals to monitor water use  
 965 over California vineyards of different climate, vine variety and trellis design. *Agricultural  
 966 Water Management*, 241, 106361. <https://doi.org/10.1016/j.agwat.2020.106361>
- 967 Lhomme, J.-P., & Elguero, E. (1999). Examination of evaporative fraction diurnal behaviour using  
 968 a soil-vegetation model coupled with a mixed-layer model. *Hydrology and Earth System  
 969 Sciences*, 3(2), 259–270. <https://doi.org/10.5194/hess-3-259-1999>
- 970 Li, S., Kang, S., Li, F., Zhang, L., & Zhang, B. (2008). Vineyard evaporative fraction based on  
 971 eddy covariance in an arid desert region of Northwest China. *Agricultural Water  
 972 Management*, 95(8), 937–948. <https://doi.org/10.1016/j.agwat.2008.03.005>
- 973 Li, Z.-L., Tang, R., Wan, Z., Bi, Y., Zhou, C., Tang, B.-H., et al. (2009). A Review of Current  
 974 Methodologies for Regional Evapotranspiration Estimation from Remotely Sensed Data.  
 975 In *Sensors*. <https://doi.org/10.3390/s90503801>
- 976 Liu, X., Xu, J., Zhou, X., Wang, W., & Yang, S. (2020). Evaporative fraction and its application in  
 977 estimating daily evapotranspiration of water-saving irrigated rice field. *Journal of  
 978 Hydrology*, 584, 124317. <https://doi.org/10.1016/j.jhydrol.2019.124317>

- 979 McNaughton, K. G., & Jarvis, P. G. (1983). Predicting effects of vegetation changes on  
 980 transpiration and evaporation. *Water Deficits and Plant Growth*. Retrieved from  
 981 <http://agris.fao.org/agris-search/search.do?recordID=US201302611148>
- 982 Minnis, P., Mayor, S., Smith, W. L., & Young, D. F. (1997). Asymmetry in the diurnal variation of  
 983 surface albedo. *IEEE Transactions on Geoscience and Remote Sensing*, 35(4), 879–890.  
 984 <https://doi.org/10.1109/36.602530>
- 985 Miranda, R. de Q., Galvncio, J. D., Moura, M. S. B. de, Jones, C. A., & Srinivasan, R. (2017,  
 986 January 24). Reliability of MODIS Evapotranspiration Products for Heterogeneous Dry  
 987 Forest: A Study Case of Caatinga [Research Article].  
 988 <https://doi.org/10.1155/2017/9314801>
- 989 Mu, Q., Heinsch, F. A., Zhao, M., & Running, S. W. (2007). Development of a global  
 990 evapotranspiration algorithm based on MODIS and global meteorology data. *Remote*  
 991 *Sensing of Environment*, 111(4), 519–536. <https://doi.org/10.1016/j.rse.2007.04.015>
- 992 Mu, Q., Zhao, M., & Running, S. W. (2011). Improvements to a MODIS global terrestrial  
 993 evapotranspiration algorithm. *Remote Sensing of Environment*, 115(8), 1781–1800.  
 994 <https://doi.org/10.1016/j.rse.2011.02.019>
- 995 Nichols, W. E., & Cuenca, R. H. (1993). Evaluation of the evaporative fraction for  
 996 parameterization of the surface energy balance. *Water Resources Research*, 29(11), 3681–  
 997 3690. <https://doi.org/10.1029/93WR01958>
- 998 Nishida, K., Nemani, R. R., Running, S. W., & Glassy, J. M. (2003). An operational remote  
 999 sensing algorithm of land surface evaporation. *Journal of Geophysical Research:*  
 1000 *Atmospheres*, 108(D9). <https://doi.org/10.1029/2002JD002062>
- 1001 Panwar, A., Renner, M., & Kleidon, A. (2020). Imprints of evaporative conditions and vegetation  
 1002 type in diurnal temperature variations. *Hydrology and Earth System Sciences*, 24(10),  
 1003 4923–4942. <https://doi.org/10.5194/hess-24-4923-2020>
- 1004 Paul, S., Banerjee, C., & Nagesh Kumar, D. (2020). Evaluation Framework of Landsat 8–Based  
 1005 Actual Evapotranspiration Estimates in Data-Sparse Catchment. *Journal of Hydrologic*  
 1006 *Engineering*, 25(9), 04020043. [https://doi.org/10.1061/\(ASCE\)HE.1943-5584.0001992](https://doi.org/10.1061/(ASCE)HE.1943-5584.0001992)
- 1007 Portela, M. M., Santos, J., & Studart, T. M. de C. (2019). Effect of the Evapotranspiration of  
 1008 Thornthwaite and of Penman-Monteith in the Estimation of Monthly Streamflows Based  
 1009 on a Monthly Water Balance Model. *Current Practice in Fluvial Geomorphology -*  
 1010 *Dynamics and Diversity*. <https://doi.org/10.5772/intechopen.88441>
- 1011 Ryu, Y., Baldocchi, D. D., Black, T. A., Detto, M., Law, B. E., Leuning, R., et al. (2012). On the  
 1012 temporal upscaling of evapotranspiration from instantaneous remote sensing  
 1013 measurements to 8-day mean daily-sums. *Agricultural and Forest Meteorology*, 152,  
 1014 212–222. <https://doi.org/10.1016/j.agrformet.2011.09.010>
- 1015 Shuttleworth, W. (1989). FIFE: The variation in energy partition at surface flux sites.
- 1016 Sobrino, J. A., Gomez, M., Jimenez-Munoz, J. C., & Oliso, A. (2007). Application of a simple  
 1017 algorithm to estimate daily evapotranspiration from NOAA–AVHRR images for the  
 1018 Iberian Peninsula. *Remote Sensing of Environment*, 110(2), 139–148.  
 1019 <https://doi.org/10.1016/j.rse.2007.02.017>
- 1020 Song, J. (1998). Diurnal asymmetry in surface albedo. *Agricultural and Forest Meteorology*,  
 1021 92(3), 181–189. [https://doi.org/10.1016/S0168-1923\(98\)00095-1](https://doi.org/10.1016/S0168-1923(98)00095-1)
- 1022 Sugita, M., & Brutsaert, W. (1991). Daily evaporation over a region from lower boundary layer

- 1023 profiles measured with radiosondes. *Water Resources Research*, 27(5), 747–752.  
 1024 <https://doi.org/10.1029/90WR02706>
- 1025 Tang, Q., Peterson, S., Cuenca, R. H., Hagimoto, Y., & Lettenmaier, D. P. (2009). Satellite-based  
 1026 near-real-time estimation of irrigated crop water consumption. *Journal of Geophysical*  
 1027 *Research: Atmospheres*, 114(D5). <https://doi.org/10.1029/2008JD010854>
- 1028 Tang, R., & Li, Z.-L. (2017). An improved constant evaporative fraction method for estimating  
 1029 daily evapotranspiration from remotely sensed instantaneous observations. *Geophysical*  
 1030 *Research Letters*, 44(5), 2319–2326. <https://doi.org/10.1002/2017GL072621>
- 1031 Tang, R., Li, Z.-L., & Sun, X. (2013). Temporal upscaling of instantaneous evapotranspiration: An  
 1032 intercomparison of four methods using eddy covariance measurements and MODIS data.  
 1033 *Remote Sensing of Environment*, 138, 102–118. <https://doi.org/10.1016/j.rse.2013.07.001>
- 1034 Tang, R., Li, Z.-L., Sun, X., & Bi, Y. (2017). Temporal upscaling of instantaneous  
 1035 evapotranspiration on clear-sky days using the constant reference evaporative fraction  
 1036 method with fixed or variable surface resistances at two cropland sites. *Journal of*  
 1037 *Geophysical Research: Atmospheres*, 122(2), 784–801.  
 1038 <https://doi.org/10.1002/2016JD025975>
- 1039 Van Niel, T. G., McVicar, T. R., Roderick, M. L., van Dijk, A. I. J. M., Beringer, J., Hutley, L. B.,  
 1040 & van Gorsel, E. (2012). Upscaling latent heat flux for thermal remote sensing studies:  
 1041 Comparison of alternative approaches and correction of bias. *Journal of Hydrology*, 468–  
 1042 469, 35–46. <https://doi.org/10.1016/j.jhydrol.2012.08.005>
- 1043 Wang, D., Liang, S., He, T., Yu, Y., Schaaf, C., & Wang, Z. (2015). Estimating daily mean land  
 1044 surface albedo from MODIS data. *Journal of Geophysical Research: Atmospheres*,  
 1045 120(10), 4825–4841. <https://doi.org/10.1002/2015JD023178>
- 1046 Wang, K., & Dickinson, R. E. (2012). A review of global terrestrial evapotranspiration:  
 1047 Observation, modeling, climatology, and climatic variability. *Reviews of Geophysics*,  
 1048 50(2). <https://doi.org/10.1029/2011RG000373>
- 1049 Yang, K., Koike, T., & Ye, B. (2006). Improving estimation of hourly, daily, and monthly solar  
 1050 radiation by importing global data sets. *Agricultural and Forest Meteorology*, 137(1), 43–  
 1051 55. <https://doi.org/10.1016/j.agrformet.2006.02.001>
- 1052 Yang, K., He, J., Tang, W., Qin, J., & Cheng, C. C. K. (2010). On downward shortwave and  
 1053 longwave radiations over high altitude regions: Observation and modeling in the Tibetan  
 1054 Plateau. *Agricultural and Forest Meteorology*, 150(1), 38–46.  
 1055 <https://doi.org/10.1016/j.agrformet.2009.08.004>
- 1056 Zhang, K., Kimball, J. S., Mu, Q., Jones, L. A., Goetz, S. J., & Running, S. W. (2009). Satellite  
 1057 based analysis of northern ET trends and associated changes in the regional water balance  
 1058 from 1983 to 2005. *Journal of Hydrology*, 379(1), 92–110.  
 1059 <https://doi.org/10.1016/j.jhydrol.2009.09.047>
- 1060 Zhang, K., Kimball, J. S., Nemani, R. R., & Running, S. W. (2010). A continuous satellite-derived  
 1061 global record of land surface evapotranspiration from 1983 to 2006. *Water Resources*  
 1062 *Research*, 46(9). <https://doi.org/10.1029/2009WR008800>
- 1063 Zhang, L., & Lemeur, R. (1995). Evaluation of daily evapotranspiration estimates from  
 1064 instantaneous measurements. *Agricultural and Forest Meteorology*, 74(1), 139–154.  
 1065 [https://doi.org/10.1016/0168-1923\(94\)02181-I](https://doi.org/10.1016/0168-1923(94)02181-I)
- 1066 Zhang, X., Jiao, Z., Dong, Y., He, T., Ding, A., Yin, S., et al. (2020). Development of the Direct-

- 1067 Estimation Albedo Algorithm for Snow-Free Landsat TM Albedo Retrievals Using Field  
1068 Flux Measurements. *IEEE Transactions on Geoscience and Remote Sensing*, 58(3),  
1069 1550–1567. <https://doi.org/10.1109/TGRS.2019.2946598>
- 1070 Zou, M., Zhong, L., Ma, Y., Hu, Y., Huang, Z., Xu, K., & Feng, L. (2018). Comparison of Two  
1071 Satellite-Based Evapotranspiration Models of the Nagqu River Basin of the Tibetan  
1072 Plateau. *Journal of Geophysical Research: Atmospheres*, 123(8), 3961–3975.  
1073 <https://doi.org/10.1002/2017JD027965>
- 1074 Zhang, Y., Kong, D., Gan, R., Chiew, F. H. S., McVicar, T. R., Zhang, Q., & Yang, Y. (2019).  
1075 Coupled estimation of 500 m and 8-day resolution global evapotranspiration and gross  
1076 primary production in 2002–2017. *Remote Sensing of Environment*, 222, 165–182. <https://doi.org/10.1016/j.rse.2018.12.031>
- 1077  
1078  
1079